Journal of Power Sources 264 (2014) 168–183

Contents lists available at ScienceDirect

Journal of Power Sources

journal homepage: www.elsevier.com/locate/jpowsour

Review

Recent progress in degradation and stabilization of organic solar cells

Huanqi Cao [a], Weidong He [a,*], Yiwu Mao [b], Xiao Lin [c], Ken Ishikawa [d,*], James H. Dickerson [e], Wayne P. Hess [f,*]

[a] School of Energy Science and Engineering, University of Electronic Science and Technology, Chengdu, Sichuan 611731, PR China
[b] Institute of Nuclear Physics and Chemistry, China Academy of Engineering Physics, Mianyang 621900, PR China
[c] School of Physics, University of Chinese Academy of Sciences, Beijing 100049, PR China
[d] Department of Organic and Polymeric Materials, Tokyo Institute of Technology, 2-12-1-S8-28 O-okayama, Meguro, Tokyo 152-8552, Japan
[e] Department of Physics, Brown University, Providence, RI 02912, USA
[f] Chemical and Materials Science Division, Pacific Northwest National Laboratory, P.O Box 999, Richland, WA 99352, USA

HIGHLIGHTS

- Reviews degradation of organic solar cells caused by water, oxygen and light irradiation.
- Describes mechanisms of a few promising ways of stabilizing organic solar cells.
- Overviews essential recent literature in stabilization of organic solar cells.

ARTICLE INFO

Article history:
Received 3 February 2014
Received in revised form
11 April 2014
Accepted 16 April 2014
Available online 10 May 2014

Keywords:
Organic solar cells
Stability
Degradation
Interface
Diffusion

ABSTRACT

Stability is of paramount importance in organic semiconductor devices, especially in organic solar cells (OSCs). Serious degradation in air limits wide applications of these flexible, light-weight and low-cost power-generation devices. Studying the stability of organic solar cells will help us understand degradation mechanisms and further improve the stability of these devices. There are many investigations into the efficiency and stability of OSCs. The efficiency and stability of devices even of the same photoactive materials are scattered in different papers. In particular, the extrinsic degradation that mainly occurs near the interface between the organic layer and the cathode is a major stability concern. In the past few years, researchers have developed many new cathodes and cathode buffer layers, some of which have astonishingly improved the stability of OSCs. In this review article, we discuss the recent developments of these materials and summarize recent progresses in the study of the degradation/stability of OSCs, with emphasis on the extrinsic degradation/stability that is related to the intrusion of oxygen and water. The review provides detailed insight into the current status of research on the stability of OSCs and seeks to facilitate the development of highly-efficient OSCs with enhanced stability.

1. Introduction

Organic solar cells (OSCs) are considered to be a green solar energy technology. OSCs are attractive mainly because they can be fabricated from various organic compounds with modifiable structures and exhibit excellent flexibility, high power conversion efficiency (PCE) under low light irradiation, and promising see-through power-generation windows. Over the course of the past few years, various aspects of organic solar cells have been extensively studied, including synthesis and application of new materials, modeling of physical processes, large-scale manufacturing, stability improvement, etc [1]. The research trajectories of OSCs have been described in various reviews [2–6].

The ultimate aim of organic solar cell research is to realize efficient solar energy conversion. In the past two decades, OSC efficiency has been remarkably improved through new approaches such as using fullerene electron acceptors [7,8], and broadening OSC absorption bands within the solar spectra [9]. The total energy output of a fabricated solar cell equals the product of its efficiency and lifetime. Therefore, stability is an important OSC property that impacts the value (yield over cost) of an OSC system as current energy production is largely limited by the low durability. Thanks to persistent efforts, our understanding of the degradation of OSCs

* Corresponding authors. Tel./fax: +86 2861831252.
E-mail addresses: weidong.he@uestc.edu.cn (W. He), iken@op.titech.ac.jp (K. Ishikawa), wayne.hess@pnnl.gov (W.P. Hess).

http://dx.doi.org/10.1016/j.jpowsour.2014.04.080
0378-7753/

Nomenclatures and acronyms

I_{ph}	light-induced electric current
I_{sh}	leakage current between electrodes
R_{sh}	shunt resistance
R_p	parallel resistance
R_s	series resistance
I_{SC}	short-circuit current
J_{SC}	short-circuit current density
V_{OC}	open-circuit voltage
P_{in}	the total power of the incident light beam
R_sA	series resistance times active area
T_{xx}	the time for PCE reaching xx% of the initial value or maximum value
t_{xx}	the related time according to J_{SC}
T50	half-shelf-life
Δc	concentration difference
OSCs	organic solar cells
PCE	power conversion efficiency
ITO	indium tin oxide
PALs	photoactive layers
HTL	hole-transport layer
ETL	electron-transport layer
BHJ	bulk-heterojunction
PHJ	planar-heterojunction
PCE	power conversion efficiency
DIB-SQ	2,4-bis[4-(*N*,*N*-diisobutylamino)-2,6-dihydroxyphenyl]squaraine
Pcs	phthalocyanines
P3HT	poly(3-hexylthiophene-2,5-diyl)
PCBM	[6,6]-phenyl-C61-butyric-acid-methyl-ester
H_2Pc	non-metal phthalocyanine
ZnPc	zinc phthalocyanine
FF	fill factor
OPV	organic photovoltaic
IEC	International Electrotechnical Commission
WVTR	water vapor transmission rate
OLEDs	organic light-emitting diodes
PEDOT	poly(3,4-ethylenedioxythiophene)
PSS	polystyrene sulfonate
PEDOT:PSS	poly(3,4-ethylenedioxythiophene):poly(*p*-styrenesulfonate)
HSCs	hybrid solar cells
MEH-PPV	poly(2-methoxy-5-(2′-ethyl-hexoxy)-1,4-phenylene-vinylene)
BCP	bathocuproine
BPhen	bathophenanthroline
LBIC	laser-beam-induced photocurrent
TOF-SIMS	time-of-flight secondary ion mass spectrometry
PBDTTPD	poly(benzo[1,2-b:4,5-b′]dithiophene-alt-thieno[3,4-*c*]pyrrole-4,6-dione
MOs	metal oxides
AZO	Al-doped ZnO
Alq3	tris-8-hydroxy-quinolinato aluminum
TPBI	1,3,5-tris(2-*N*-phenylbenzimidazolyl) benzene
P3(TBP)HT	poly[3-(6-{4-*tert*-butylpyridiniumyl}-hexyl) thiophene-2,5-diyl]
$PC_{71}BM$	[6,6-phenyl-C71-butyric acid methyl ester
PBDTTP	poly({4,8-di(2-ethylhexyloxyl)benzo[1,2-b:4,5-b′] dithiophene}-2,6-di yl)-alt-({5-octylthieno[3,4-c] pyrrole-4,6-dione}-1,3-diyl)
APTES	3-aminopropyltriethoxysilane
PBDTTT-C	poly{(4,8-bis-(2-ethylhexyloxy)-benzo[1,2-*b*;4,5-*b*′] dithiophene}-2,6-diyl-alt-(4-(2-ethylhexanoyl)-thieno[3,4-*b*]thiopene)-2,6-diyl]
PDMAEMA	poly(2-*N*,*N*-dimethylaminoethyl methacrylate)
DSSC	high-efficiency dye-sensitized solar cell
ODE	ordinary differential equation
MDMO-PPV	poly[2-methoxy-5-(3,7-dimethyloctyloxy)-1,4-phenylene-vinylene]
MeO-TPD	*N*,*N*,*N*′,*N*′-tetrakis(4-methoxyphenyl)-benzidine
PEG	polyethylene glycol
PCDTB	poly[*N*-9′-heptadecanyl-2,7-carbazole-alt-5,5-(4′,7′-di-2-thienyl-2′,1′,3′-benzothiadiazole)]

has been significantly deepened. Numerous structures have been developed to protect OSCs from degradation and the shelf lives of unencapsulated organic solar cells have been improved to thousands of hours. In addition, the working lifetime, of encapsulated organic solar cells under continuous irradiation, has improved. These efforts have made organic solar cells increasingly attractive. Jørgensen et al. systematically reviewed the degradation and stabilization studies of OSCs until 2012 [10].

Recently, more efficient stabilization methods have been reported, such as the aluminum–titanium top cathodes [11], and the modified ITO bottom cathodes [12]. These methods improve the half-shelf-lives of unencapsulated OSCs fabricated with morphologically stable materials to about one year in air. This review focuses on these new developments. We cover the following topics in sequence: how OSCs work, how OSCs degrade including the effects of oxygen, water, and light irradiation, how to stabilize OSCs, and finally an overview of relatively stable OSCs appearing in recent literature. The reviewed papers are mainly based on two morphologically stable structures of CuPc/C_{60} and P3HT:PCBM.

2. Working principle

A single-junction OSC comprises five or six layers stacked on the surface of a supporting substrate, which is normally a piece of glass or transparent plastic. These five or six layers include a transparent conductive electrode (normally indium–tin-oxide, ITO), a hole-transport layer (HTL), one or two photoactive layers (PALs) composed of an electron donor and an electron acceptor, an electron-transport layer (ETL), and a top metal electrode (normally Al or Ag). The HTL also functions as an electron-blocking layer, or an exciton-blocking layer. Similarly, the ETL also functions as a hole-blocking layer. For simplicity, buffer layers are denoted HTL and ETL as shown in Fig. 1. An extra encapsulation film is sometimes employed. In some cases, the PALs are doped or modified with

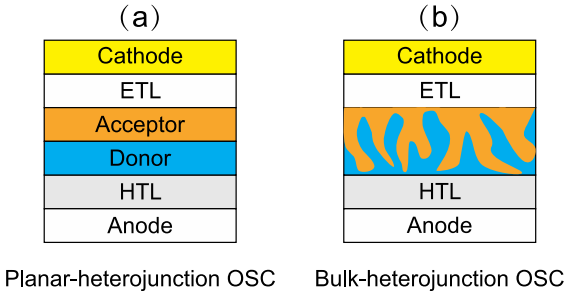

Fig. 1. Schematic diagrams of a planar-heterojunction OSC (a) and a bulk-heterojunction OSC (b).

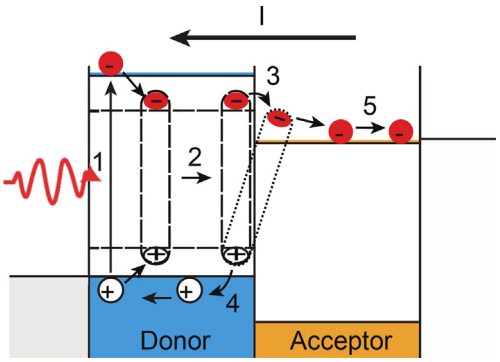

Fig. 2. Photocurrent generation mechanism in active layers of an organic solar cell. 1) A photon excites an electron to the higher energy level (LUMO), to form an exciton; 2) The exciton diffuses to the D–A interface; 3) charge transfer at the interface forms a geminate electron–hole pair; 4) delocalization of the interfacial electron–hole pair; 5) separated charges diffuse to electrodes, driven by the chemical or electrical potential.

functional dopants. Over 200 small-molecular or oligomer organic semiconductors used in OSCs were recently reviewed (see Ref. [5]).

OSCs are categorized by whether or not the electron donor (D) and acceptor (A) layers form a planar heterojunction or are intermixed during fabrication, to form a bulk-heterojunction (BHJ) or planar-heterojunction (PHJ), as illustrated in Fig. 1. In BHJ-OSCs, electron donor and acceptor materials are intermixed during fabrication. For the PHJ-OSCs, multilayer semiconductors are deposited in sequence. According to which side is close to the substrate, OSCs can be categorized as conventional (anode directly on substrate) or inverted (cathode directly on substrate). Despite the structural difference, working principles of OSCs are essentially the same. Fig. 2 displays the OSC mechanism, in which the donor and acceptor absorb and convert incident light into photocurrent.

OSCs must overcome the following obstacles to generate photocurrents:

1. The absorption of photons, which generates tightly-bound excitons instead of free charge pairs;
2. The low diffusion lengths of excitons in organic semiconductors;
3. The recombination of excited charges at the D–A interface;
4. The cooling of hot charge-transfer excitons at the D–A interface [13,14];
5. The low or imbalanced carrier mobilities in semiconductors.

A widely used one-diode equivalent circuit of an irradiated solar cell, including two parasitic resistances is shown in Fig. 3. A generalized Shockley equation depicting the photocurrent in Fig. 3 is expressed in Eq. (1),

$$I - I_0 \times \left[e^{e\times(V-I\times R_s)/nk_BT} - 1\right] - \frac{V - I\times R_s}{R_\rho} + I_{\text{light}} = 0 \qquad (1)$$

where I is the current in the diode, V is the applied external bias, I_0 is the saturation current, T is the temperature, R_s is the serial resistance, R_ρ is the parallel resistance, n is the ideality factor, k_B is the Boltzmann constant, and I_{light} is the light-induced electric current. The serial resistance (R_s) is a parasitic resistance originating from the resistance of bulk semiconductors and connections of electrodes. R_s should ideally be zero. Too high an R_s or too low an R_{sh} causes the failure of a solar cell. The parameters of an OSC appearing in Fig. 3a can be extracted from one single I–V curve [15,16]. The actually measured I–V curves tested under light irradiation are typically deviated from the ideal curve [16,17].

Short-circuit current (I_{SC}) is defined as the current at $V = 0$, corresponding to the intersection of the I–V curve with the current axis. Short-circuit current density (J_{SC}) is often used in literature. The open-circuit voltage (V_{OC}), defined as the voltage at $I = 0$, corresponds to the intersection of the I–V curve with the voltage axis. The maximum power P_{max} corresponds to the maximum area of the square in the fourth quadrant. Fill factor (FF) is calculated according to $FF = P_{max}/(I_{SC} \times V_{OC})$. FF describes the deflation of the I–V curve in the fourth quadrant. Power conversion efficiency (PCE) is defined as the ratio of P_{max} to the total power of the incident light beam P_{in}: $PCE = P_{max}/P_{in}$.

Qi and Wang summarized factors influencing V_{OC} and FF [18,19]. Briefly, V_{OC} is determined by the summation of the offsets of energy levels where excited charges are separated, and is also influenced by temperature, illumination intensity, material microstructure, etc. FF loss is typically indicated by the appearance of the S-shape I–V curve, which is caused by the electric field formed by accumulated charges in devices. Scharber et al. suggested that a donor material with a HOMO of 5.4 eV, and a bandgap of 1.4 eV is most suitable for coupling with fullerene to achieve a theoretical PCE up to 10% [20].

Chen et al. reported a small-molecular OSC with V_{OC} of 0.86 V and PCE of 6.3% by co-depositing 2,4-bis[4-(*N*,*N*-diisobutylamino)-2,6-dihydroxyphenyl] squaraine (DIB-SQ) and C_{70}. The squaraine derivative has a bandgap of 1.7 eV and a HOMO of 5.3 eV. They also noted that PCE of this system is not very sensitive to donor/acceptor blending ratio and film thickness [21].

Phthalocyanines (Pcs) are common OSC electron donors, not only due to their strong absorption in the visible part of the solar spectra, but also due to their extraordinarily high thermal and

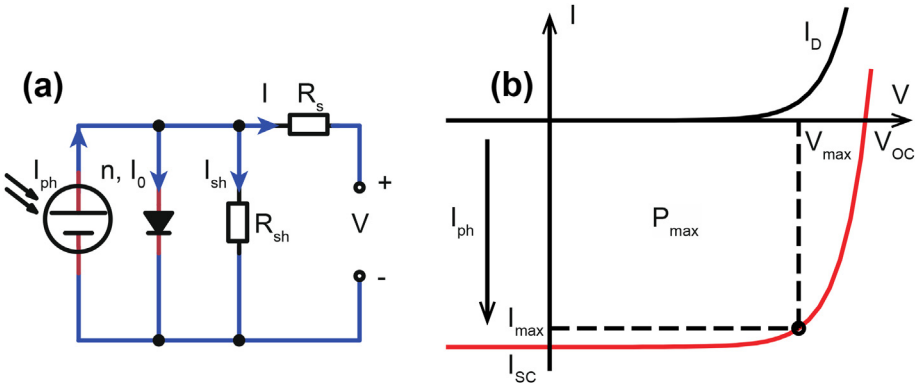

Fig. 3. (a) Equivalent circuit of a single-diode solar cell under light irradiation. (b) Dark (black) and illuminated (red) I–V curves of an ideal solar cell ($n = 1$, $R_s = 0$ and $R_{sh} = \infty$). (For interpretation of the references to color in this figure legend, the reader is referred to the web version of this article.)

chemical stability and environmental safety. Copper phthalocyanine (CuPc), non-metal phthalocyanine (H_2Pc) and zinc phthalocyanine (ZnPc) are popular Pcs that are used in OSCs. The latter two Pcs are normally used to fabricate the so-called *p-i-n* OSCs, *i.e.* vacuum-processed BHJ-OSCs. Sakai and Hiramoto fabricated *p-i-n* OSCs with PCE of 5.3% under simulated 74.2 mW cm^{-2} solar light, despite a relatively low V_{OC} of 0.4 V. They used a very thick (960 nm) blending *i*-interlayer composed of H_2Pc:C_{60}. They annealed the device during codeposition to enhance the device performance, and pointed out that high purities of the two source materials are indispensable to the increased thickness of the blending interlayer [22]. Interestingly, Wagner et al. suggested that a CuPc:C_{60} blend was not suitable for such a *p-i-n* structure [23].

The most studied polymer in BHJ-OSCs is the morphologically stable regioregular poly(3-hexyl thiophene) (P3HT) [24]. It acts as the donor and is usually blended with [6,6]-phenyl-C61-butyric-acid-methyl-ester (PCBM) to constitute the PAL. Chemical structures of CuPc, C_{60}, P3HT and PCBM are shown in Fig. 4.

3. Degradation of OSCs

The degradation of OSCs means the degradation of device capability (particularly the PCE) and not necessarily chemical degradation of the composite materials. Depending on the significance of air exposure, the degradation of OSCs can be divided into intrinsic and extrinsic degradation. The former is caused by the thermal interdiffusion of constituent species inside OSCs, while the latter is caused by the intrusion of air. Both types of degradation are mass-transport processes (diffusion). The metal–organic interfaces are the major interfaces where degradation occurs, even in OSCs that are stored in an inert atmosphere [25].

3.1. Intrinsic degradation

The intrinsic degradation of OSCs originates from thermal diffusion of constituent materials at interfaces. It includes phase separation at the organic–cathode interface, where an intrinsic stress exists [26], phase segregation at semiconductor interfaces [27], and inter-diffusion at buffer layer interfaces [28]. Morphological evolution inside the BHJ-OSCs has been reviewed [29], and physically modeled [30].

Besides PCE, V_{OC} is another important factor that demands high stability in practical use. V_{OC} can be unstable during aging at a high temperature [31]. This may come from the interaction between fullerene and aluminum, which increases the work function of aluminum [32], likely forming a Schottky junction between the acceptor and the cathode. Aging tests, at a high temperature, accelerate thermal diffusion of aluminum because aluminum has a low recrystallization temperature. The intermixing of aluminum and organic layers during deposition is detrimental to the interfacial charge transport [33]. Hermenau et al. proposed that the interdiffusion between aluminum or ITO and organic layers after fabrication causes negligible degradation [34].

One recent report shows that organic photovoltaic (OPV) modules from Konarka passed the International Electrotechnical Commission (IEC) chamber tests. The three parallel tests include: 1000 h damp heat test at 85 °C and 85% RH, 200 cycles of thermal cycling test from 40 °C to 85 °C, and a sequential test comprising of a UV precondition, 50 cycles of TC test, and 10 cycles of humidity freeze test from 40 °C to 85 °C and 85% RH. These Konarka modules were encapsulated with flexible barriers with a low water vapor transmission rate (WVTR) of 5×10^{-3} g m^{-2} d^{-1} at 65 °C, 85% RH. Such high intrinsic stability might be correlated with the epoxy cross-linking agent used at the PAL–cathode interface. Replacing the flexible barriers with glass further improved the stability. They accordingly attributed the observed degradation of modules to extrinsic degradation caused by water intrusion [35].

Using morphologically stable materials including P3HT:PCBM and CuPc/C_{60} as the PALs, the degradation of devices is mainly the extrinsic degradation caused by the intrusion of air (oxygen and water). The extrinsic degradation can be accelerated by light irradiation. In the following subsections, we discuss the influence of oxygen, water and light irradiation on the stability of OSCs.

3.2. Oxygen in OSCs

Intrusion of oxygen and water are the two main causes of extrinsic degradation. The relative significance between these two factors is frequently argued in literature. OSCs and organic light-emitting diodes (OLEDs) are based on similar materials but are degraded by different mechanisms. In OLEDs, water causes the major extrinsic degradation [26]. Nonetheless, oxygen is dominant in the extrinsic degradation in some OSCs due to the following factors. First, fullerene is hydrophobic and does not react with water. Aluminum, however, can become passivated against water-induced corrosion in the presence of fullerene [36]. Second, electron-transport properties of fullerene suffer much from the exposure to oxygen in air [37]. Third, oxygen increases the work functions of metals by forming surface dipoles [38], which deteriorate the performance of conventional OSCs, but may temporarily enhance the performance of inverted OSCs [39].

Norrman et al. fabricated OSCs with a structure of ITO/ZnO/PCBM:P3HT/PEDOT:PSS/Ag, and found that oxygen causes more significant degradation of encapsulated OSCs, whereas both water and oxygen cause serious degradation of unencapsulated OSCs (Fig. 5). The top PEDOT:PSS layer impedes the intrusion of air more efficiently than the aluminum cathodes used in conventional OSCs [24].

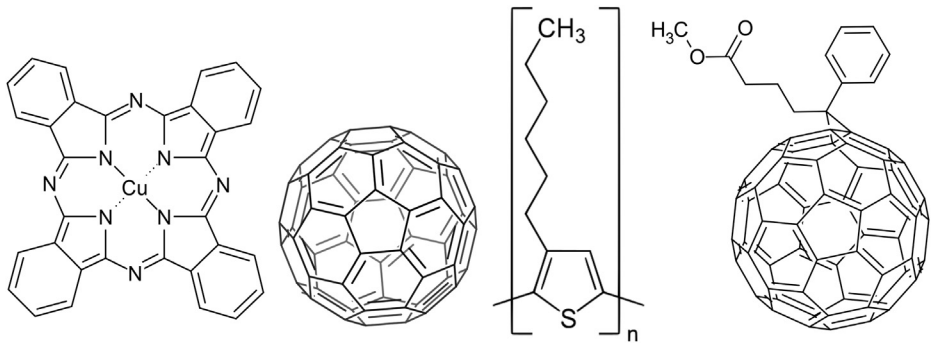

Fig. 4. Chemical structures of four common organic semiconductors used in OSCs. Left to right: CuPc, C_{60}, P3HT, and PCBM.

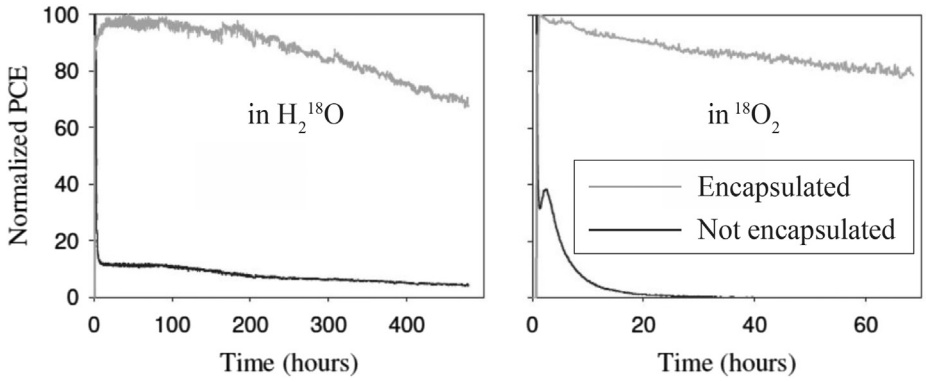

Fig. 5. Degradation of encapsulated and unencapsulated devices under continuous illumination (330 W m^{-2}, AM1.5G, 65 ± 2 °C) in an oxygen-free isotopically labeled humid atmosphere (65 ± 2% RH, left) or in a dry (<0.1% RH) isotopically labeled oxygen atmosphere (20% $^{18}O_2$, 80% N_2, right) [24].

Oxygen may also constructively affect the electronic properties of other constituent materials in OSCs. Oxygen is normally a p-type dopant (electron trap) in semiconductors [40,41], whereas oxygen vacancies serve as electron donors [42]. Therefore, the electronic properties of the layers in which holes are the majority carrier may temporarily be enhanced upon exposure to oxygen.

Lira-Cantu et al. fabricated inverted organic–inorganic hybrid solar cells (HSCs) with a structure of ITO/oxides/MEH-PPV/Ag, and found that applying the semiconductor oxides, such as ZnO, or TiO_2, or Nb_2O_5, requires the presence of oxygen for the correct functioning of the semiconductor oxides as electron acceptors. These HSCs degrade drastically under light irradiation in vacuum, but are partially recovered upon exposure to air [43]. They proposed that the degradation is due to the removal of oxygen from the Nb_2O_5 surface under UV irradiation, whereas the recovery of performance in air comes from the reuptake of oxygen [44]. Later, they proposed another oxygen-related mechanism to explain the photo-activation of OSCs, in which ZnO was used as the ETLs. In this case, however, the photoconductivity of ZnO was proposed to be activated upon exposure to UV irradiation [45].

Conventional OSCs generally suffer from extrinsic degradation in air [46]. To overcome this issue, researchers typically fabricate inverted OSCs. In inverted OSCs, the sequence of the layers in Fig. 1 is inverted. The inverted structure can protect OSCs from rapid degradation in air to some extent (Fig. 6). Even in inverted OSCs, oxygen intrusion into the fullerene layer still causes rapid degradation [47]. The top buffer layers in inverted OSCs, which are composed of PEDOT:PSS, might degrade due to the phase separation in the presence of oxygen [24]. Wang et al. showed that the shelf lives of inverted small-molecule OSCs (CuPc/C_{60}) could be greatly improved to about 950 h in air [32]. In this case, the ambient oxygen takes a longer time to diffuse to the bottom fullerene layer.

Andreasen et al. quantitatively studied the time-dependent oxygen concentration in OSCs, and found that oxygen accumulates in the active layers, with a linear time dependence, leading to OSCs degradation (Fig. 7) [49].

Besides increasing the work function of metals, oxygen also oxidizes active metals. This may influence the interfacial charge transport, at different degradation stages, depending on oxide thickness and electric conductivity. If the oxide layer is (semi-) conducting, or if it is insulating but too thin to block electrons to transport, exposure to oxygen may not influence the device performance. However, if the oxide is insulating and thick, the electron tunneling will diminish at the interface and degrade performance.

In some labs, as-fabricated PALs are transferred to vacuum for the deposition of top electrodes. The PALs are exposed to air and adsorb oxygen during the transfer. The strong oxygen affinity of fullerene impedes the removal of adsorbed oxygen [50]. Tavakkoli et al. reported that pre-exposure, before the deposition of the top electrodes, causes more serious device degradation [51]. Roesch et al. found that the working pressure of the vacuum chamber in

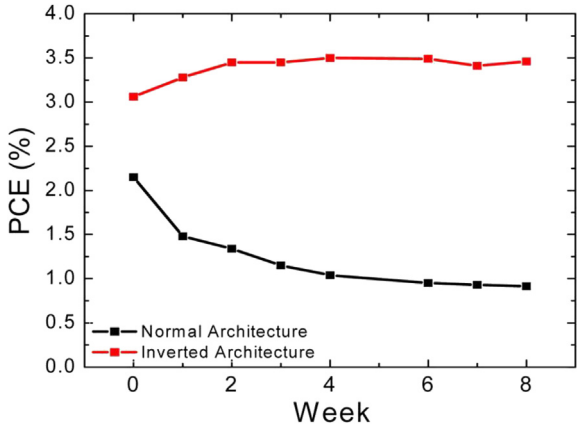

Fig. 6. Comparison between conventional and inverted OSCs [48].

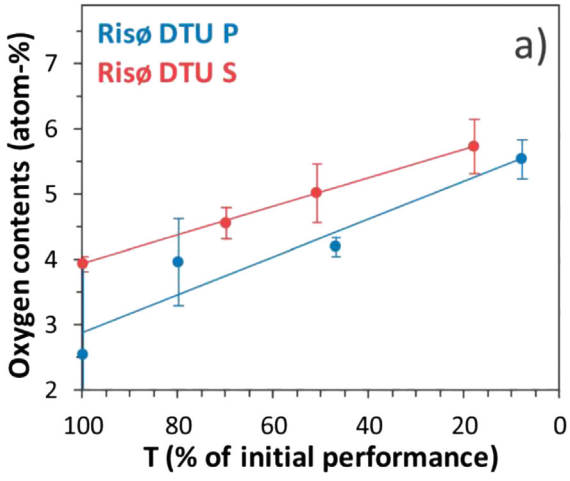

Fig. 7. Oxygen contents as a function of loss in performance. The Risø DTU P has a structure of UV-filer/PET/ITO/ZnO/PCBM:P3HT/PEDOT:PSS/Ag grid/UV-filter. The Risø DTU S has a slightly modified P3HT polymer P3HT-*co*-P3AcET, with part of the hexyl side chains oxidized to ester [49].

which the top electrodes are deposited influences the stability of fabricated devices [52].

3.3. Water induced degradation

According to a number of reports, the effect of oxygen on the extrinsic degradation of OSCs is less significant than that of water [34,53–55]. It is well known that the surface of aluminum in dry air is immediately passivated by the formation of an ultrathin oxide layer of ca. 2–3 nm, which is thin enough for charges to tunnel. However, in a humid environment, the thickness of oxide doubles and therefore blocks charge tunneling. Unlike the above-mentioned constructive/destructive effects of oxygen, almost no constructive effect of water on OSCs has ever been suggested. The ambient humidity has been suggested to play an important role in the degradation of OSCs, particularly those with hydrophilic materials, like PEDOT:PSS [56], or bathocuproine (BCP), or bathophenanthroline (BPhen) [34]. The physical swelling or recrystallization of these materials, as well as the corrosion of active cathodes in the presence of these hygroscopic materials accelerates the degradation of the devices by forming insulating interfaces or interfacial voids.

Petersen et al. reported a distinct divergence between oxygen-induced degradation and water-induced degradation of OSCs, in which a polymeric donor having ester groups on the side chain was used. The OSCs show very high resistance to oxygen, but very low resistance to water [54]. Norrman et al. found that 90% RH induces the rapid degradation of BHJ-OSCs. Using labeled $H_2^{18}O$, they found that water diffuses through the grain boundaries in the aluminum cathode even in the dark. The penetrated water continues diffusing vertically throughout the PAL to the ITO layer. The vertical diffusion of water in the PAL was accelerated by light irradiation [56].

It should be noted that water in air generally affects OSCs seriously at high RH. This suggests that the effect of humidity is nonlinear with RH. Voroshazi et al. proposed an exponential relation between RH and the shelf lives of unencapsulated OSCs at room temperature (Fig. 8). The degradation of these BHJ-OSCs was attributed to the oxidation of active cathodes caused by water intruding from device edges. In the same report, they inserted 5 nm fullerene layers between the PALs and Yb/Al cathodes, without noticing any impairment of stability in air [55].

It is usually assumed that the water-induced degradation is related to PEDOT:PSS, the most common HTL in both conventional and inverted OSCs. In conventional OSCs, PEDOT:PSS is adjacent to ITO, and the chemical reaction between ITO and PEDOT:PSS is often suggested as the cause of device degradation [57]. However, in general, PEDOT:PSS accelerates the degradation of unencapsulated devices, not due to its acidity, but due to its hygroscopicity [55]. If the moisture adsorbed by PEDOT:PSS is released, it can continue to diffuse through the active layers and finally corrode the active electrodes. On the other hand, in inverted OSCs, PEDOT:PSS is adjacent to the top anodes which are usually composed of relatively stable metals like silver. The influence of humidity on stability in this case is the deterioration of the PEDOT–PSS–PAL interfaces [24].

By inserting a thin titanium layer, which possesses an extraordinarily high corrosion resistance beneath the aluminum cathode, the corrosion resistance of the aluminum cathode is greatly enhanced. AlTi–OSCs with HTLs of PEDOT:PSS were more stable than those with MoO_3 in ambient atmosphere (Fig. 9). On the contrary, Al–OSCs with HTLs of PEDOT:PSS were less stable than those with MoO_3, which is consistent with the reports we now discuss.

Yamanari et al. probed the laser-beam-induced photocurrent (LBIC) of different cells with HTLs of PEDOT:PSS or MoO_x or without HTL, and found that the degradation of OSCs in the presence of PEDOT:PSS is caused by the accelerated oxidation of aluminum. The device with PEDOT:PSS suffers seriously from the peripheral intrusion of air from device edges (Fig. 10) [58]. Similarly, Sun et al. fabricated OSCs with PEDOT:PSS or MoO_x as HTLs and TiO_x as ETLs, and found that the MoO_x devices are more stable than the PEDOT:PSS devices [59].

These results show negligible degradation that could be attributed to the acidity of PEDOT:PSS. The reduced shelf lives of Al–OSCs containing PEDOT:PSS are doubtlessly correlated with the accelerated corrosion of the active cathodes, *viz.* aluminum.

Hermenau et al. quantitatively studied the degradation of small-molecular OSCs with different encapsulation barriers. They found that a 100 nm thick aluminum cathode possesses a WVTR of 8×10^{-4} g m^{-2} d^{-1} (glass barrier used in this report has a WVTR of 3.9×10^{-5} g m^{-2} d^{-1}) at 45 °C, 5.5% RH. They concluded that approximately 10 mg m^{-2} water is the dose corresponding to the half-shelf-life (T50) of an OSC [60]. Assuming that this dose is valid

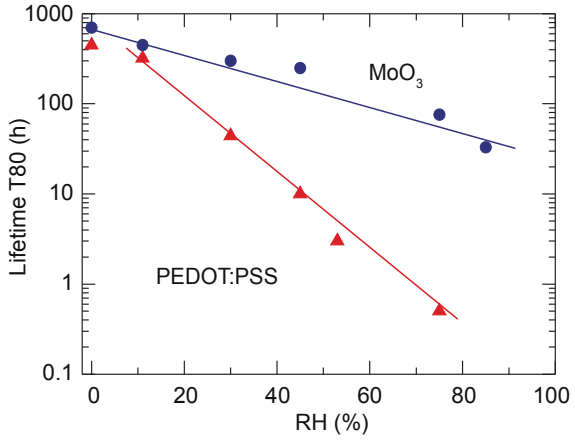

Fig. 8. Lifetime (T80, defined as the time for PCE drops to 80% of its initial value) of BHJ-OSCs at different humidity levels with PEDOT:PSS (red triangles) and MoO_3 (blue circles) [55]. (For interpretation of the references to color in this figure legend, the reader is referred to the web version of this article.)

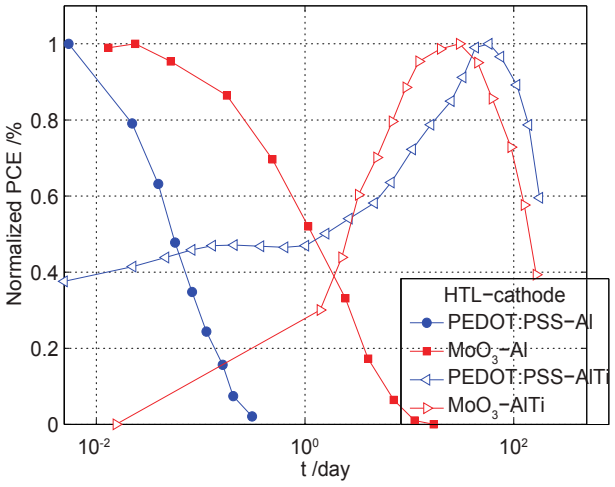

Fig. 9. Comparison of four OSCs with structures of ITO/HTL (PEDOT:PSS or MoO_3)/CuPc/C_{60}/BCP/cathode (Al or Ti/Al). The devices were not encapsulated and stored in ambient air (20 °C, 60% RH on average). Large shunts initially shorted the MoO_3–AlTi–OSC (red triangle). (For interpretation of the references to color in this figure legend, the reader is referred to the web version of this article.)

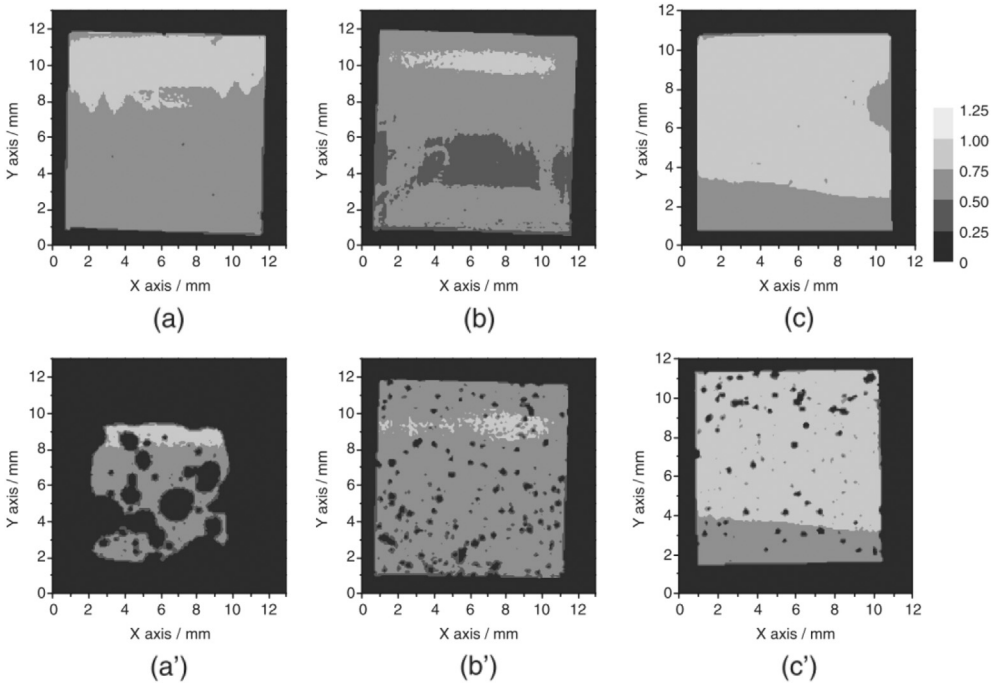

Fig. 10. LBIC images for (a–c) fresh and (a′–c′) degraded cells with different types of buffer layer stored in the dark in ambient air for approximately 300 h: (a, a′) PEDOT:PSS, (b, b′) MoO_x, and (c, c′) no buffer layer [58].

for other structures at room temperature, the AlTi bilayer cathode, with a T50 of 250 days [11], has a WVTR of 4×10^{-5} g m^{-2} d^{-1} at 20 °C, 60% RH. Considering the relatively higher stability of BPhen compared to BCP [51,61], the actual WVTR of the AlTi bilayer cathode might be even lower.

However, the bilayer cathodes could be ruptured by high humidity, as shown in Fig. 11. Exposure to high humidity (RH >90%) for a few hours resulted in the rupture of the cathodes. More importantly, the rupture mainly occurred in areas where LiF was deposited (region A). Such ruptures were probably formed by the corrosion of aluminum at the cathode-organic interfaces. LiF (region A) and BCP (region C) caused much more serious rupture compared to bare C_{60} (region B). The bottom PEDOT:PSS layer seemed to have no relation to the moisture-induced rupture, since region B is intact. This was presumably a consequence of the above-mentioned passivation of aluminum by fullerene [36].

These results are consistent with the previous finding that water mainly diffuses into OSCs through the grain boundaries in the aluminum cathodes instead of through peripheral edges [56]. It again confirms that PEDOT:PSS alone does not cause the degradation of OSCs if the cathodes are corrosion-proof.

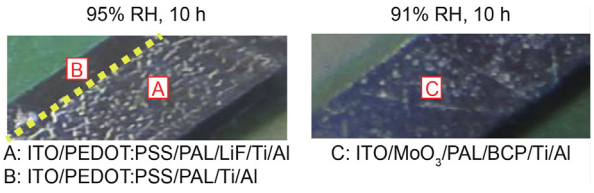

Fig. 11. Photographs of ruptured AlTi cathodes after exposure to high humidity for 10 h (PAL = CuPc/C_{60}). The RH was monitored with a USB logger. The two distinguishable regions A and B in the left figure were formed due to the non-uniformity of LiF. Both devices degraded almost totally in high humidity (left: 100% lost; right: 90% lost), and recovered slowly when stored subsequently in normal air (left: ~15% recovered; right: >50% recovered).

3.4. Light irradiation induced degradation

Except the above-mentioned photo-activation of some OSCs [10,45], light irradiation normally accelerates the degradation of OSCs in the following three ways. First, the thermal effect of strong light irradiation might accelerate the intrinsic degradation of OSCs [27]. Second, light irradiation causes the photo-degradation of organic semiconductors [62]. TOF-SIMS analysis shows that light irradiation causes the oxidation of organic semiconductors nearby the organic–aluminum interface [63]. Third, light irradiation accelerates the diffusion of both oxygen and water in the bulk of PAL [50,56,63,64].

One intriguing phenomenon is that, light-induced degradation can usually be partially recovered in the dark [41,65]. This recovery is temperature independent [66]. When aluminum was used as the cathodes, such recovery was observed only on an unencapsulated OSC, but not on encapsulated OSC, suggesting that it is probably related to oxygen [64]. The photo-induced 'fatigue' and the subsequent recovery in the dark might be related to the photo-excitation and extinction of singlet oxygen in fullerene, respectively [67]. Singlet oxygen has an energy level 0.98 eV higher than the triplet ground-state [68], and will accordingly affect the charge transfer at the donor–acceptor interface more significantly. Fullerene also quenches singlet oxygen, which explains the relatively short recovery time of the photo-fatigued OSCs in dark (30 min) compared to the lifetime of singlet oxygen (60 min).

Andreasen et al. quantitatively probed the influence of light irradiation and thermal annealing on the amount of oxygen uptaken by PALs (Fig. 12). Annealing in the dark reduces the oxygen amount (purple curve), whereas illumination increases the oxygen amount (green curve). Long-term light irradiation further causes the reaction (deep trapping) of oxygen (red curve). The decreases of oxygen contents as a function of time in vacuum were attributed to the reversible formation of a charge transfer complex between P3HT and oxygen [49]. Note that light also causes another similar well-known reversible trapping of oxygen in fullerene [50,69,70].

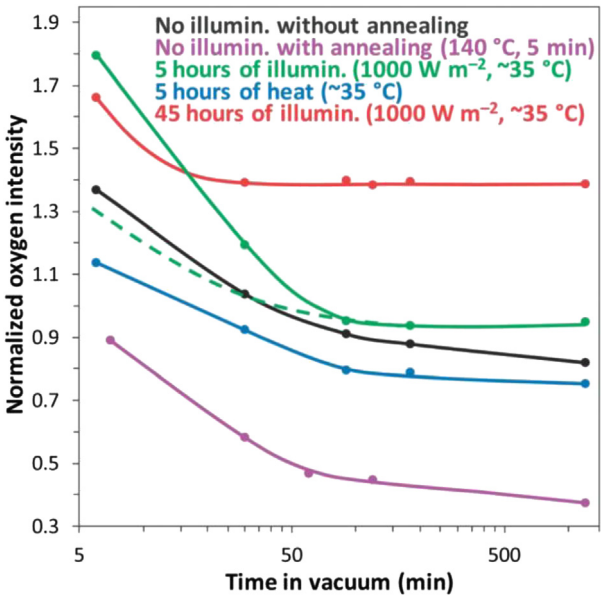

Fig. 12. Normalized oxygen intensity of the film as a function of time in vacuum for spin-coated P3HT:PCBM films [49].

It might be argued that the light-induced degradation depends on the intensity of light irradiation. However, Hermenau et al. found that there is no clear correlation between the light irradiation intensity (24–478 mW cm^{-2}) and the degradation of both encapsulated and unencapsulated OSCs [60].

4. Ways of stabilizing OSCs

As mentioned above, OSCs need to be intrinsically and extrinsically stable. In addition, flexible OSCs should be mechanically stable. Crystalline structures of rigid materials in OSCs can be irreversibly damaged under small-angle bending. To be flexible, ITO electrodes can be replaced with organic conducting materials, like PEDOT:PSS [71], or single-walled carbon nanotubes [72]. Finally, the organic semiconductors used in OSCs need to be chemically stable under solar irradiation [62,73].

Stabilization of OSCs is structure dependent. In this section, we first briefly discuss a few ways of improving the intrinsic stability of OSCs, and then we discuss a few common ways of improving the extrinsic stability of conventional and inverted OSCs. Two general ways are to use metal oxides as the buffer layers, and silver as the top anodes. We further discuss two newly developed effective stabilization methods, with each only applicable to one type of structure. Titanium–aluminum can be used as the top cathode in conventional structures, whereas modified ITO can be used as the bottom cathode in inverted structures.

4.1. Improving the intrinsic stability

There are several ways of improving the intrinsic stability of OSCs. One can improve the intrinsic (thermal) stability by enhancing the cathode-PAL interface using cross-linked epoxy [35].

Another way is to use multilayer cathodes. For conventional structures, Reese et al. found that inserting alkaline earth metals like Ca or Ba beneath the Al cathodes can enhance the efficiency and shelf stability of OSCs stored in a glove box [74]. For inverted structures, Zimmermann et al. found that Cr/Al/Cr trilayer cathodes could protect OSCs under continuous light irradiation in an inert atmosphere. They also concluded that Ti/Al/Ti trilayer cathodes are less stable than the Cr/Al/Cr cathodes again under inert atmosphere [75]. Note that CrO_x was also used in OSCs to improve the extrinsic stability [76].

Improving the purity of the component materials can also improve the intrinsic stability of OSCs. Mateker et al. fabricated devices with a structure of ITO/PEDOT:PSS/PBDTTPD:PCBM/Ca/Al and found that the shelf stability of these devices stored in an inert atmosphere is significantly improved through the purification of PBDTTPD. The improved shelf stability was attributed to the removal of low-molecular-weight organic contaminants in PBDTTPD. They further proposed that the small organic impurities might diffuse to the PAL-cathode interface, causing S-shape features (kinks) in the reverse bias region of *I–V* curves upon reaction with the metal cathode or interlayer [77].

For extrinsic stability, virtually all stabilization approaches rely on this simple principle: hindering the diffusion of oxygen/water into the acceptor–cathode interface, and facilitating the effusion of oxygen/water from this interface to render OSCs more stable in air. Two ways are available. One is to develop flexible encapsulation films with low oxygen transmission rates, low WVTRs and strong UV absorption. The other way is to enhance the air resistance of OSCs by using functional layers. We focus on recent developments of the second method to improve the stability of OSCs without encapsulation.

4.2. Metal oxides as buffer layers

Semiconducting metal oxides (MOs) are popular buffer layers that have been widely used beneath the top electrodes to improve the extrinsic stability of both conventional and inverted OSCs. Three commonly used metal oxides are titanium oxides (ETL), zinc oxides (ETL) and molybdenum oxides (HTL). According to Fick's first law of diffusion, the diffusion rate through a metal (M) layer is proportional to the concentration difference (Δc) on both sides (Fig. 13). Oxygen usually has a low diffusion constant in MO compared to M, thereby forming a large concentration gradient across the MO layer. The higher concentration of oxygen at the M–MO interface (Fig. 13, c3) compared to the M–PAL interface (Fig. 13, c2) sufficiently reduces Δc, thereby reducing the diffusion rate of oxygen from air to PAL.

ZnO and TiO_x are two popular ETLs that have been widely used in both conventional and inverted OSCs. Both materials can be processed from solution [48,78], and are thus compatible with large-scale manufacturing. TiO_x is typically prepared from precursors solved in isopropyl alcohol, followed by repeated heating. Li et al. showed that TiO_x scavenges oxygen under light irradiation, which is probably related to the photo-oxidation of bound organic moieties [79]. Prior to the application of TiO_x to OSCs, Hänsel et al. fabricated OSCs using TiO_2 as cathode buffer layers (different from DSSC). The TiO_2 was deposited by heating Ti_3O_5 in a vacuum

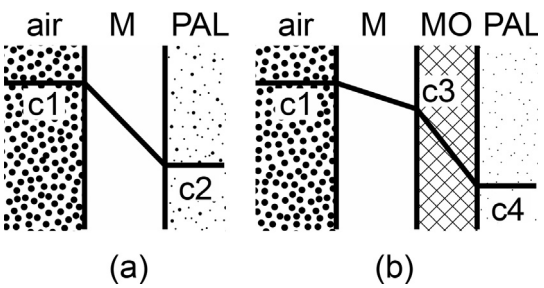

Fig. 13. Illustration of the steady-state oxygen concentration gradient nearby the top electrode of an OSC in air, without (a), and with (b) metal oxide.

chamber with an oxygen partial pressure of 2.5×10^{-3} Pa. Note that no fullerene was used in their devices. Under continuous irradiation in vacuum, the OSCs with TiO_2 were less stable than those without TiO_2 [80]. This reveals that, without oxygen deficit, titanium oxides cannot stabilize OSCs in the inert atmosphere.

You et al. compared the stability of encapsulated devices with ETLs of ZnO or Cs doped TiO_2, and found that devices based on the former are more stable [81]. Besides ZnO, zinc oxides are also used in OSCs in doped forms, like Al-doped ZnO (AZO) [82], or Sr and Ba doped ZnO [83]. Liu et al. fabricated BHJ-OSCs based on AZO anodes, which exhibit strong absorption in the UV part of solar spectra. As a result, these devices show similar PCE with those based on ITO anodes, but exhibit much improved UV resistance [84].

Molybdenum oxides are commonly used HTLs in OSCs [85,86]. Recently, Zhang et al. found that, MoO_x is thermally unstable and releases oxygen from the surface upon thermal annealing. As a consequence, a surface dipole is generated, which further up-shifts the energy levels. In organic semiconductor devices, this might form a charge transport barrier between MoO_x and organic semiconductors [87]. This thermal instability explains the aforementioned relatively low shelf stability of AlTi–OSCs with HTLs of MoO_3, compared to those with PEDOT:PSS. It should be noted that the refractive index matching between the MoO_x (compared to PEDOT:PSS) layer and the PAL may increase the light absorption in the PAL, thereby possibly increasing the PCE [59].

4.3. Silver as the top anode

Besides aluminum, silver has also been widely used to fabricate electrodes of OSCs, by vacuum deposition or printing. Tavakkoli et al. found that PHJ-OSCs with silver cathodes are more stable than those with aluminum cathodes in air. They attributed this divergence to the morphological refinement of silver compared to aluminum [51].

As a noble metal, silver electrodes are normally more stable than aluminum electrodes in air. However, silver is more suitable for the anodes since the work function of silver can be improved upon exposure to oxygen. Lloyd et al. fabricated inverted OSCs without fullerene, with ZnO as ETLs and silver as top anodes. They found that these devices can be stable in air over one year, but with a relatively low PCE of 0.1% [39].

One important factor in manufacturing OPV modules is the cost. Printing and roll-to-roll processes are the most economical ways of manufacturing large-scale thin-film electronic devices. Krebs et al. analyzed the manufacturing cost of OPV modules in the roll-to-roll process. Silver paste was used as the top electrode while ITO was used as the bottom electrode. The highest materials cost in the roll-to-roll manufacturing comes from the ITO layer, followed by the PAL, the ZnO layer, and the silver paste layer [47]. The application of silver paste is more desirable than other printable metals (Mo, Cr, Ti, and Au) for large-scale production [24].

Nevertheless, Rösch et al. studied the surface imaging of many OSCs along with the degradation, and pointed out that the electromigration of silver in the OSCs causes the degradation of the devices [88].

4.4. Titanium–aluminum as the top cathode for conventional OSCs

Combined with aluminum, titanium significantly improves the stability of conventional OSCs. Although it is still unknown to what extent titanium layers oxidize during deposition in vacuum, one advantage of this technique is that titanium and aluminum can be processed in the same vacuum system, saving fabrication time. The high air-stability of AlTi–OSCs does not come from the oxygen-vacancy in titanium. Evidence is that OSCs with cathodes composed of 100 nm titanium show much lower stability compared to those with 2 nm titanium and 100 nm aluminum [89]. In this subsection, we discuss the functionalities of titanium in OSCs.

Titanium surfaces exposed in air are immediately oxidized to TiO_2, which is an n-type anion-defective oxide, through which oxygen ions can interstitially diffuse. By adding specific doping atoms like Al, Nb, etc., the diffusion rate of oxygen in titanium can be significantly decreased by forming a dense metal oxide layer [90,91]. In AlTi–OSCs, the aluminum–titanium interfaces need to be passivated to prevent air intrusion. The passivation consumes (scavenges) oxygen residing in the bottom layers or intruding from the ambient atmosphere. However, such an oxygen scavenging process is slow as discussed below.

Diffusivity depends on temperature following the Arrhenius relation: $D = D_0 \exp[-Q/(RT)]$, where Q is the activation energy, and D_0 is the pre-exponential constant. The diffusivity of oxygen in α-Ti (the stable form of titanium at <1155 K) is approximately $0.0067 \times 10^{-12420/T}$ m^2 s^{-1} at 860–1490 K. The diffusivity of oxygen in the surface scale (rutile) of titanium is approximately $0.087 \times 10^{-12110/T}$ m^2 s^{-1} at 866–1033 K [92]. The diffusivity of aluminum in α-Ti is approximately $0.0013 \times 10^{-16650/T}$ m^2 s^{-1} at 900–1155 K. [91] Supposing that the Qs and D_0s are also valid at room temperature (300 K), the estimated $D_{\text{oxygen in α-Ti}}$, $D_{\text{oxygen in rutile}}$, and $D_{\text{Al in α-Ti}}$ are 9.0×10^{-23}, 1.4×10^{-20}, and 1.4×10^{-37} nm^2 h^{-1}, respectively. We may accordingly infer that the diffusion of oxygen and aluminum in titanium is very slow at room temperature. Oxygen that diffuses to the Al–Ti interfaces and further passivates the interfaces should mainly come vertically from the organic side, instead of laterally from the titanium layers.

We thus propose the following model. Aluminum extracts oxygen from titanium oxides [93], so the aluminum–titanium interface is expected to be more efficient in scavenging oxygen. On the other hand, oxygen forms a concentration gradient in titanium as a consequence of the slow diffusion. The titanium layer should be thin enough to prevent the intrusion of air before the formation of a

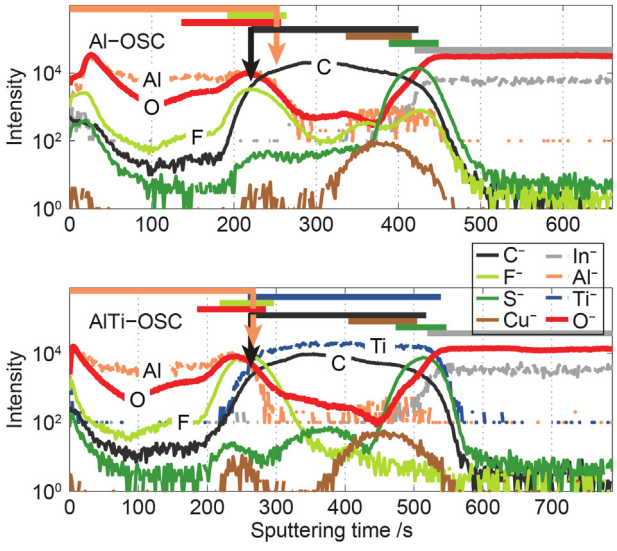

Fig. 14. TOF-SIMS depth profiles of anions sputtered from an Al–OSC (top) and an AlTi–OSC (bottom, structure on the left of Fig. 11) after exposed in air over two months. The color bars on the top of each figure represent regions cut at fifth of maximum intensities of the related anions. Edges of Al and C_{60} bars were indicated with the vertical arrows [11]. (For interpretation of the references to color in this figure legend, the reader is referred to the web version of this article.)

Table 1
Conventional BHJ-OSCs.

Structure	Area cm^2	J_{SC} mA cm^{-2}	V_{OC} V	FF	PCE %	R_sA Ω cm^2	Sealing method	Storage condition	T_{xx} or t_{xx} h	T50/T80 h	Notes	Ref
ITO/PEDOT:PSS/P3HT:PCBM/Al	0.6	–	–	–	0.25	–	PEN-based foils; two-component epoxy resin	D, r.t., 35–50% RH	T50 6000	6000	Flexible substrate (1.5% PCE for same size glass substrate);	[104]
ITO/PEDOT:PSS/MDMO-PPV:PCBM/Al	17.1	0.12	1.1	0.26	0.035	–			T54 3000	3261		
ITO/PEDOT:PSS/P3HT:PCBM/Al	10	3.9	0.48	0.26	0.48	–	Al plate; reinforced epoxy	LL (on average)	T65 8592		Occasionally used under solar illumination	[105]
Ag/PEDOT:PSS/ZnO/PCBM:P3HT/PEDOT:PSS/Ag	186	5.45	4.76	0.56	1.05	–	UV curing adhesive, lower WVTR barrier foils	D, r.t., 20–35%	T80 2800	7000	Roll-to-roll	[106]
								LL, 20 mW cm^{-2}, 30 °C, 12.5% RH	T80 700–1000			
								L, 70 °C, 12.5% RH	T80 500–1300			
								O, r.t.	T80 1500			
ITO/HTL*/P3HT:PCBM/Ca/Al	233 (total)	0.073	29	0.51	1.09	–	Cavity glass; UV-curable sealant; getter	L (Xe lamp)	T80/T50 2600/8100	/2600	PCE certificated by NREL; T80/T50 were estimated according to the given degradation rate	[107]
								50% L–D duty	T80/T50 4350/13,500		T80/T50 were estimated according to the given degradation rate	
ITO/MeO-TPD:$C_{60}F_{36}$/ZnPc:C_{60}/C_{60}/BPhen/Al	0.064	7.3	0.54	0.56	1.4	–	None	N_2, 33 mW cm^{-2}, 49 °C, RH = 0	t80/t50 405/2700		–	[34]
		7.4	0.54	0.56	1.4	–	None	O_2, 33 mW cm^{-2}, 49 °C, RH < 17%	t80/t50 43/74			
		7.6	0.54	0.56	1.5	–	None	H_2O:N_2, 33 mW cm^{-2}, 49 °C, 65% RH	t80/t50 6.0/11			
ITO/PEDOT:PSS/P3HT:PCBM/ZnO(sol–gel + NPs)/Al	–	7.6	0.52	0.4	1.59	26.7	None	D, r.t.	T75 1872	3744	Tungsten-halogen lamp, 100 mW cm^{-2}	[108]
ITO/PEDOT:PSS/P3HT(98% RR):PCBM/Al	0.1	9.3	0.54	0.52	2.5	–	None	N_2	T7 480		–	[109]
ITO/PEDOT:PSS/P3HT(94% RR):PCBM/Al		8.8	0.54	0.48	2.3	–			T79 2880			
ITO/MoO_x/P3HT:PCBM/Al	1.0 or 1.2	8	0.58	0.58	2.7	–	None	D, r.t.	T69 500	806	–	[58]
ITO/PEDOT:PSS/P3HT:PCBM/ Mg:Ag/Ag	–	10.4	0.58	0.49	2.96	–	None	D, N_2	T62 1008		Ca/Al or Ba/Al are the most efficient/stable cathodes in vacuum, on the shelf	[25,74]
Ag		9	0.4	0.37	1.33				T16 1008			
Ca/Al		10.4	0.6	0.61	3.81				T89 1008			
								L, N_2	T50 140	/45		
								10% L, N_2	T85 200			
ITO/MoO_3/P3HT:PCBM/Yb/Al (150 nm)	0.13	9.8	0.58	0.63	3.6	–	None	D, r.t., 30–40% RH	T80 600	1500	T80 of PEDOT:PSS-OSC is 10 h	[56]
ITO/PEDOT:PSS/P3HT:PCBM/SPPO1/Al	0.04	12	0.56	0.56	3.8	–	Glass, getter	L, 60 °C	T87 10			[28]
ITO/PEDOT:PSS/P3HT:PCBM/CrO_x/Al	0.02	11.2	0.58	0.61	3.9	–	None	–	T50 168	168	CrO_x was formed by depositing 5 nm Cr in a low vacuum chamber	[76]
ITO/PEDOT:PSS/P3HT:PCBM/PEG-200/Al	–	10.3	0.59	0.66	4	1.5	None	D, r.t., 50% RH	T80/T50 500/1800	1800	PEG vertically diffuses to the top and form beneficial ohmic contacts with Al;	[110]
ITO/PEDOT:PSS/P3HT:PCBM/Al		8.35	0.49	0.54	2.3	12.5						
ITO/PEDOT:PSS/P3HT:PCBM/Ca/Al		–	–	–	–	–			T80/T50 75/360	360		

(*continued on next page*)

Table 1 (*continued*)

Structure	Area cm^2	J_{SC} mA cm^{-2}	V_{OC} V	FF	PCE %	R_sA Ω cm^2	Sealing method	Storage condition	T_{xx} or t_{xx} h	T50/T80 h	Notes	Ref
											normalization	
ITO/PEDOT:PSS/P3HT:PCBM/TiO_x/Al	–	9.5	0.6	0.7	4	7	None	L	t94		PCEs were not given. 7 nm TiO_x was the optimal thickness	[111]
									100			
ITO/NDP2:MeO-TPD/ZnPc:C_{60}/NDN1:C_{60}/*Au*/NDP2:MeO-TPD/ZnPc:C_{60}/NDN1:C_{60}/Al	0.062	7.5	1.01	0.55	4.1	–	Glass; epoxy	185 mW cm^{-2}, 50 °C D, 85 °C	T97/T57 1464/2000 T20 336		Abrupt drop of efficiency after 1464 h V_{OC} also decreased	[31]
ITO/PEDOT:PSS/P3HT:PCBM/TiO_x/Al (150 nm)	0.045	10.8	0.62	0.61	4.1	–	None	–	T50 120	120	Two orders higher than without TiO_x	[78]
ITO/PEDOT:PSS/PCPDTBT:PCBM/TiO_x/PEDOT:PSS/P3HT:PC_{71}BM/TiO_x/Al	–	7.5	1.2	0.63	5.5	–	None	N_2, r.t. L, N_2	T85 3500 T70/T60 40/100		Tandem structures	[112]
ITO/MoO_x/PCDTBT:PC_{71}BM/TiO_x/Al	0.12 (0.20 active)	10.9	0.89	0.67	6.5	–	None	–	T50 720	720	MoO_x-OSC is more stable than PEDOT:PSS-OSC	[59]
ITO/PEDOT:PSS/PBDTTPD (high M_n, purified)/PCBM/Ca/Al (150 nm)	–	11	0.95	0.7	7.3	–	None	D, N_2	t94 2664		Purity & M_n influence the stability	[77]

passivation layer. This model agrees well with the fact that AlTi—OSCs with eight-nanometer Ti are less stable than those with thinner Ti [11].

Titanium diffuses into the organic layers in AlTi—OSCs (Fig. 14). Titanium tends to cluster on fullerene [94], instead of interstitially diffusing into octahedral interstices in the fullerene lattice like alkali metals [95]. This ensures that the initially deposited atomic layers of titanium probably exclusively occupy the grain boundaries of fullerene. This tendency is important because it retains the structure and therefore the electronic properties of fullerene. Besides, the filling of grain boundaries in fullerene slows down the diffusion of gases, which proceeds more favorably through grain boundaries.

Replacing BCP with relatively stable candidates like tris-8-hydroxy-quinolinato aluminum (Alq3) [96], 1,3,5-tris(2-*N*-phenyl-benzimidazolyl) benzene (TPBI) [61], or BPhen [51] can further improve the half-shelf-lives of the AlTi—OSCs to a time scale of a year.

4.5. Modified ITO as the bottom cathodes for inverted OSCs

The stability of inverted OSCs can be improved by modifying the bottom ITO electrodes with ultrathin polycationic layers [35]. Polymers containing amino groups universally reduce the work function of ITO and thus ITO is applicable as the bottom cathode in semiconductor devices [71].

Worfolk et al. reported inverted OSCs with a structure of ITO/[P3(TBP)HT/PEDOT:PSS]$_{5.5}$/PC_{71}BM:PBDTTPD/V_2O_5/Al, with PCE of 4.4% and T97/T78 of 1080 h/1580 h in ambient air [97]. Interestingly, the degradation curve shows a tendency of acceleration with storage time in air. This is probably correlated with the final arrival of air from the top layers to the bottom cathode/acceptor layers, or the failure of the top electrode.

Song et al. fabricated inverted OSCs with 3-aminopropyltriethoxysilane (APTES) modified ITO as the bottom cathode. The APTES reduces the work function of ITO from 4.9 eV to 4.4 eV. The device structure was ITO/APTES/PCBM:PBDTTT-C/Ag, with PCE of 4.83%. No buffer layer was used beneath the top silver anode. They found that the T80 of the fabricated devices stored on the shelf in air is 720 h [98].

Tan et al. fabricated inverted OSCs with a structure of ITO/PDMAEMA/PCBM:P3HT/MoO_3/Ag, in which the polymer Poly(2-*N*,*N*-dimethylaminoethyl methacrylate) (PDMAEMA) reduces the work function of ITO from 4.38 eV to 3.94 eV. These devices exhibit an averaged PCE of 3.2% and super high stability in air. T94 is 1344 h in air under 56 cycles of 8 h of AM1.5 irradiation and 16 h of dark storage. They further compared the stability of devices based on polymer-modified ITO with those based on ITO/ZnO nanoparticles (NPs) and found that the former are more stable [12]. These results further confirm the importance of the cathode-acceptor interface in the stability of OSCs.

5. Overview of lifetimes in literature

Due to the extremely intricate structures of modern OSCs, shelf/aging stability of fabricated devices involves a number of variables. Besides the large variation in component materials, the large variation in encapsulation/storage/test conditions, and more importantly, the scattered initial efficiencies of as-fabricated devices make comparison among lifetimes only meaningful for those of the same PALs, with similar initial performances, and under the same encapsulation/storage conditions and test procedures. A consensus has been reached [99], with regard to accounting for variations in the encapsulation/storage/test conditions reported in literature.

Table 2
Inverted BHJ-OSCs.

Structure	Area cm^2	J_{SC} mA cm^{-2}	V_{OC} V	FF	PCE %	R_sA Ω cm^2	Sealing method	Storage condition	T_{xx} or t_{xx} h	T50/T80 h	Notes	Ref
ITO/ZnO/PCBM:P3HT/Ag	–	7.2	0.31	0.32	0.7	–	None	D, r.t.	T50 (half maximum PCE) 5500–6000	5750	Each test lasted 3 min; 100 mW cm^{-2} tungsten–halogen lamp; even longer lifetime was given with unknown efficiency.	[39]
ITO/ETL/PCBM:P3HT/tPP/Ag	(Modules)	0.49	5.6	0.58	3	–	Two 3 M PET/PEN films (5×10^{-3} g/(m^2 day) WVTR)	85 °C; 85% RH 65 °C; 85% RH 85 °C; 85% RH	T80 1800 T80 9000 T90/T80 1000/1800		IEC chamber test Test in TÜV	[35] Roll-to-roll; PET substrate; UV protection films
							Two glass plates; 5 cm edge sealing	85 °C; 85% RH	T100/T90/T80 1500/2500/3600	/3600		Water diffusion after 1700 h from edges caused the degradation
ITO/ZnO(NP)/PCBM: P3HT/MoO_3/Ag	–	10.2	0.57	0.53	3.05	–	None	–	T115 1344	Very long	ZnO was solution processed; stored in air, and tested in N_2	[48]
ITO/MoO_3/P3HT:PCBM/ZnO/Al		6.3	0.53	0.66	2.19				T80/T50 100/550	550		
Cr/Al/Cr/PCBM:P3HT/PEDOT: PSS(200 nm)/Au	–	8	0.61	0.64	3.1	–	Glass; UV-curing adhesive	*L*, 50 °C	T82 1500	/1687	UV-reduced illumination; unstable without encapsulation; thinner PAL	[75]
Ti/Al/Ti/PCBM:P3HT/PEDOT: PSS(200 nm)/Au		8.1	0.61	0.62	3.1				T59 1500	/100	device is more stable, but with compromised PCE	
					3			*L* (75 mW cm^{-2})	T52 4700			
ITO/ZnO(sprayed)/PCBM: P3HT/PEDOT:PSS/Ag	0.38 (mask)	9.6	0.6	0.55	3.17	4.6	None	D, r.t.	T80 720	1800	Spin, spray, sputter coatings are equivalent	[103]
ITO/PEI/PCBM:P3HT/PEDOT: PSS/Ag (150 nm)	0.1	9.8	0.56	0.57	3.2	–	None	D	T100/T70 720/2448	4080	Inverted structure; tested in N_2; averaged over 5 devices	[71]
ITO/PDMAEMA/PCBM: P3HT/MoO_3/Ag	–	9.1	0.57	0.62	3.2	–	None	56 cycles of 1/3L + 2/3D	T94 1344	11,200	Estimated as shelf stability (linear decay)	[12]
ITO/ZnO(NPs)/PCBM:P3HT/MoO_3/Ag		9.1	0.56	0.65	3.3				T79 1344	3200		
ITO/[P3(TBP)HT/PEDOT: PSS]$_{5.5}$/PCBM:P3HT/V_2O_5/Al		9.2	0.55	0.6	3.5	–	None	N_2	T83 8760		eLbL assembled HTLs; tested in air	[97]
ITO/[P3(TBP)HT/PEDOT: PSS]$_{5.5}$/PC_{71}BM:PBDTTPD/V_2O_5/Al	0.16 × 4	8.9	0.89	0.57	4.4			D, r.t.	T97/T78/T50 1080/1580/2500	2500	T50 was estimated with linear extrapolating	
ITO/ZnO(NPs)/PCBM: P3HT/PEDOT:PSS/Ag	–	10.7	0.62	0.54	3.61	4	None	r.t.	T80 960	2400	–	[113]
ITO/ZnO/PCBM:PBDTTT-C/Ag	0.38	11.3	0.76	0.5	4.33	3.9	None	D, r.t.	T80 720	1800	Both devices are more efficient/stable than bare ITO; APTES suppresses Indium diffusion	[98]
ITO/APTES/PCBM:PBDTTT-C/Ag		12.4	0.76	0.5	4.83	2.9						
ITO/ZnO/PC_{71}BM:PTB7/MoO3/Ag	0.1	14.7	0.72	0.69	7.3	2	Glass; epoxy	–	T96 840	10,500	ZnO, TiO_2:Cs processed in N_2 and air, respectively; DIO was added to the polymer; tested in N_2	[81,114]
ITO/TiO2:Cs/PC_{71}BM:PTB7/MoO3/Ag		14.2	0.71	0.63	6.4	4			T87 840	3230		
ITO/PEDOT:PSS/PTB7:PC_{71}BM/Ca/Al		14.5	0.74	0.69	7.4	–			T70 240	400		
FTO/TiO_2/$CH_3NH_3PbI_3$/HTM/Au	0.29	20	0.99	0.73	15	–	50-μm-thick hot-melting polymer; microscope coverslip	L (LED, 100 mW cm^{-2}), 45 °C	T80 500	/500	DSSC; the weathering tested cell had an initial PCE of 8.8%	[100]

Table 3
Conventional PHJ-OSCs.

Structure	Area cm^2	J_{SC} mA cm^{-2}	V_{OC} V	FF	PCE %	R_sA Ω cm^2	Sealing method	Storage condition	T_{xx} h	T50 h	Notes	Ref
ITO/ZnPc/C_{60}/C_{60}: alkanoyloxybenzene/Al	–	–	0.47	0.40	–	–	Glass, getter, epoxy	10 mW cm^{-2} 475 nm LED	T39 1269		The active area was not given.	[115]
ITO/PEDOT: PSS/CuPc/C_{60}/BPhen/Ag	0.20	2.4	0.33	0.20	0.15	–	None	D	T50 2160	2160	Vacuum break before cathode deposition may cause slight degradation	[51]
ITO/PEDOT: PSS/CuPc/C_{60}/LiF/Ti/Al	0.07	1.8	0.47	0.32	0.27	–	None	LL (~1 mW cm^{-2}), r.t., 60% RH	T100 7200	18,000	PCE was very low (~0.1%) initially and reached maximum after approximately 300 days.	This work
ITO/CuPc/C_{60}/Alq3/Au	0.01	3.6	0.32	0.41	0.47	–	None	r.t.	T50/T30 (1176)/3024	1176	PCE at 1176 h was ambiguous, according to other parameters.	[116]
ITO/B6C/PEDOT: PSS/CuPc/C_{60}/BCP/Al	0.04	4.2	0.49	0.50	1.02	–	Glass, epoxy	D, r.t.	T58 2352	2800	B6C suppresses Indium diffusion.	[57]
ITO/PEDOT: PSS/CuPc/C_{60}/BCP/Ti/Al	0.07	4.4	0.48	0.57	1.2	2.2	None	LL (~1 mW cm^{-2}), r.t., 60% RH	T80/T50 960/6000	6000	Averaged over two devices	This work
ITO/CuPc/C_{60}/Alq3/Al	0.075	6.03	0.51	0.52	2.11	–	None	–	T50 61	61	Alq3-OCS was 150 times more stable than BCP-OSC; 75 mW cm^{-2}	[96]
ITO/CuPc/C_{60}/TPBI/Al	0.09	6.2	0.49	0.58	2.32	–	None	r.t.	T50 33	33	BCP-OSC is unstable due to recrystallization; 75 mW cm^{-2}	[61]
ITO/Pentacene/C_{60}/BCP/Al	0.1	11.1	0.45	0.57	2.8	–	None	D, r.t.	T94 6145	51,208	Stored in air; tested in N_2 under Xe lamp (100 mW cm^{-2}); these devices were 'encapsulated' by Al_2O_3 (200 nm)	[117]

The efficiency and stability are also influenced by the size of the active area [55,76]. In general, enlarging the active area leads to lower efficiency but higher stability. This suggests that for some devices, extrinsic degradation is also influenced by air diffused from peripheral edges.

We compared the stability of devices in the literature, each of which involves at least one stabilization method. We separately compare the stability of conventional BHJ-OSCs (Table 1) and inverted BHJ-OSCs (Table 2), and the stability of conventional PHJ-OSCs (Table 3) and inverted PHJ-OSCs (Table 4). For comparison, performances of a newly reported high-efficiency dye-sensitized solar cell (DSSC) are listed at the end of Table 2 [100].

In Tables 1–4, the sizes of active areas, the initial values of key parameters (J_{SC}, V_{OC}, FF and PCE), the encapsulation/storage/test conditions, and the lifetimes (shelf or aging) of devices are listed. Besides the four key parameters of each device, series resistance R_sA (series resistance times active area), which reflects how easy electric charges can transport at interfaces, is also listed. Note that R_sA is a temperature/light intensity dependent parameter [18] and can be extracted by various methods. Light induced degradation of OSCs has been suggested to be a consequence of the photo-absorption rather than the photocurrent [101]. Whether the circuit was opened, shorted or kept at maximum power points during the light irradiation did not influence the stability [80,102]. The related devices were stored under the following conditions during the idle periods of testing: L means continuous simulated solar light, LL means low light, D means dark, O means outdoor, and r.t. means room temperature. The default ambient condition is in air, unless noted.

We roughly estimated some of the parameters from related curves appearing in the literature, by linear interpolation/extrapolation. The degradation curves of OSCs under continuous light irradiation may either decay exponentially, or experience sudden catastrophic failures due to air leakage [31,45]. T_{xx} represents the time for PCE reaching xx% of the initial value (ISOS definition [99]) or maximum value (e.g. Ref. [103]) as illustrated in Fig. 15, while t_{xx} represents the related time according to J_{SC}.

PCE usually decays exponentially under continuous light irradiation. However, different storage conditions and aging temperatures cause much different degradation rates. Furthermore, as mentioned above, continuous irradiation sometimes causes recoverable fatigue of devices. Both make it difficult to compare among aging lifetimes in different papers. We estimated the 80% aging lifetimes of a few devices with an exponential decay model: $T80 = \ln 1.25/[\ln 100 - \ln(xx)] \times T_{xx}$. For example, supposing that T94 of a device is 100 h, its T80 is then $\ln 1.25/[\ln 100 - \ln(94)] \times 100\ \text{h} \approx 361$ h. Note that some degradation curves are double-exponential decays. This means that the degradation perhaps follows a second-order homogeneous linear ordinary differential equation (ODE) of $y'' + ay' + by = 0$, where a and b are constant (open squares in Fig. 15).

On the other hand, the stability of devices stored on the shelf reflects the durability of devices in ambient air. The shelf stability has two major variables. One is the total amount of light irradiation received by each device during storage and intermittent tests. The other is the ambient humidity. Supposing that influences from both are negligible, the shelf stability can then be compared among devices. We estimated the half-shelf-life of some devices by a linear decay model: $T50 = 50/(100 - xx) \times T_{xx}$. Using this model to calculate T50 from a relatively large xx (for example $xx > 90$) might lead to over-estimation, because many devices are degradation-free in the initial period, followed by accelerated degradation (triangles in Fig. 15) [97].

It is interesting to note that the curvatures of both types of degradation curves, *i.e.* exponential-like and linear decays can be

Table 4
Inverted PHJ-OSCs.

Structure	Area cm^2	J_{SC} mA cm^{-2}	V_{OC} V	FF	PCE %	R_sA Ω cm^2	Sealing method	Storage condition	T_{xx} h	T50 h	Notes	Ref
AZO/PTCDI/PHT/Alq3/Au	0.03	2.24	0.36	0.45	0.39	–	None	r.t.	T110 960	–	FF increased in air	[82]
ITO/Alq3/C_{60}/CuPc/Au	0.09	3.4	0.35	0.44	0.76	–	None	–	T50 1500	1500	75 mW cm^{-2}	[40]
ITO/Alq3/C_{60}/CuPc/C_{60} (5 nm)/Al	0.09	3.5	0.43	0.39	0.78	–	None	r.t.	T50 950	950	The inserted ultrathin C_{60} layer is indispensible; 75 mW cm^{-2}	[32]

roughly interpreted by a lateral diffusion model [64]. The model concept is simple: oxygen is assumed to be the dominant components leading to degradation, and is (boldly) assumed to diffuse laterally from submicroscopic pinholes in OSCs. Along with diffusion, the contaminated area is de-activated due to the strong charge trapping effect of oxygen. According to Fick's second law of diffusion, the contaminated area surrounding the oxygen source increases in radial size linearly with time (linear decay, open circles in Fig. 15). On the other hand, the diffusivity of oxygen in fullerene increases under light irradiation, likely leading to rapid degradation. However, since oxygen is also immobilized by various photo-assisted oxidations under light irradiation, the lateral diffusion will become slowed with time (exponential-like decay), or even cease if the immobilization is strong enough to compensate diffusion.

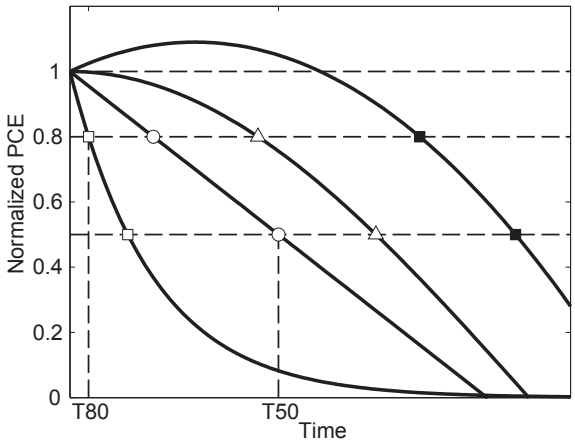

Fig. 15. Examples of four types of degradation curves as well as the 80% aging life (T80) and half-shelf-life (T50).

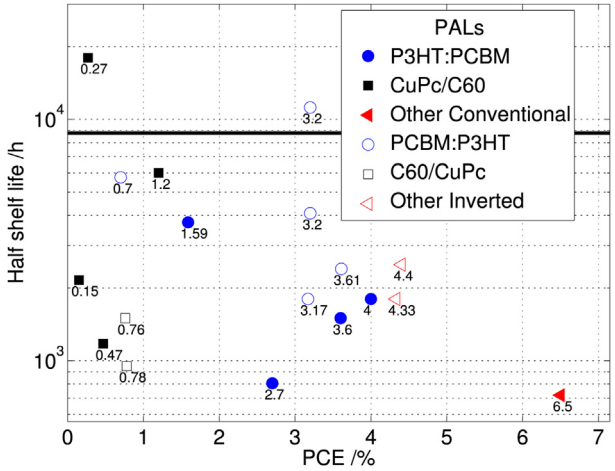

Fig. 16. Performances of unencapsulated OSCs exposed in air. Note that a few reports in which only T100 or even higher T_{xx} was mentioned were not included. The black horizontal line represents one year. The noted numbers are PCE × 100. The related details can be found according to the related PCE in tables. The top 3.2% device was tested under cycle tests [12].

Normalized PCE–t curves are often used to show the relative degradation rates among devices. Nevertheless, for OSCs with the same materials and the same encapsulation/storage/test procedures, lifetimes depend significantly on the initial PCEs. A device with a lower PCE often surpasses its initial PCE, reaches its maximum efficiency a few hours or even months after fabrication (solid squares in Fig. 15), and therefore be more stable. It is therefore suggestive to calculate the lifetime based on the maximum, instead of the initial PCE in this case. A plausible way of avoiding error is to compare the integrals of PCEs over time. A detailed mechanism describing the initial increase of performance is yet to be developed. It is probably related to the evolution of interfacial morphology, which is not optimized initially, or due to the oxygen scavenging by active metal cathodes.

PCE and T50 of unencapsulated OSCs with T50 longer than one month (720 h) are shown in Fig. 16. Solid and hollow symbols represent conventional OSCs and inverted OSCs, respectively.

6. Conclusions

We review recent developments of the degradation/stabilization study of OSCs. Up-to-date understandings of the degradation of OSCs caused by oxygen, water and light irradiation are described. A few effective ways of stabilizing OSCs are reviewed. Additionally, essential information of OSCs appearing in recent literature is overviewed for an easy comparison.

The significance of oxygen and water on the degradation of OSCs is situation-dependent. As a p-type dopant, oxygen generally causes degradation by affecting the acceptor materials and cathodes of active metals. Oxygen also occasionally enhances the device performance by modifying the work function of donor materials and anodes of inactive metals. The oxygen content in the photoactive layers increases linearly with the loss in device performance.

On the other hand, as a polar solvent, water causes the degradation of OSCs mainly by corroding active cathodes. Hygroscopic materials like PEDOT:PSS accelerate this process. Besides, water induces morphological changes of constituent materials like BCP, forming undesirable voids, which impair interfacial charge transports. The lifetimes of OSCs decrease exponentially with increasing RH in the ambient environment.

Light irradiation may activate some OSCs in which metal oxides are used as the cathode buffer layers. However, it normally causes degradation by accelerating oxidation, or by accelerating the diffusion of oxygen and water. Light irradiation causes the reversible degradation of OSCs. The light-induced degradation has little correlation with the light intensity.

To improve the stability of OSCs, numerous strategies are available. The key is to enhance the cathode-acceptor interface. For inverted OSCs, we can use polymer-modified ITO as the bottom cathodes and Ag as the top anodes with appropriate oxides as buffer layers. For conventional OSCs, aluminum–titanium bilayer cathodes as the top cathodes can be employed. Unfortunately, neither ITO nor titanium–aluminum is compatible with the large-scale roll-to-roll manufacturing. Therefore, further investigation of roll-to-roll compatible and air-stable cathodes is still urgently demanded for further improvements of the stability of OSCs.

References

[1] R. Søndergaard, M. Hösel, D. Angmo, T.T. Larsen-Olsen, F.C. Krebs, Mater. Today 15 (2012) 36.
[2] G.A. Chamberlain, Sol. Cells 8 (1983) 47.
[3] H. Spanggaard, F.C. Krebs, Sol. Energy Mater. Sol. Cells 83 (2004) 125.
[4] B.C. Thompson, J.M.J. Fréchet, Angew. Chem. Int. Ed. 47 (2008) 58.
[5] A. Mishra, P. Bäuerle, Angew. Chem. Int. Ed. 51 (2012) 2020.
[6] N. Yeh, P. Yeh, Renew. Sustain. Energy Rev. 21 (2013) 421.
[7] S.H. Park, A. Roy, S. Beaupre, S. Cho, N. Coates, J.S. Moon, D. Moses, M. Leclerc, K. Lee, A.J. Heeger, Nat. Photonics 3 (2009) 297.
[8] G. Yu, J. Gao, J.C. Hummelen, F. Wudl, A.J. Heeger, Science 270 (1995) 1789.
[9] J. You, L. Dou, K. Yoshimura, T. Kato, K. Ohya, T. Moriarty, K. Emery, C.-C. Chen, J. Gao, G. Li, Y. Yang, Nat. Commun. 4 (2013) 1446.
[10] M. Jørgensen, K. Norrman, S.A. Gevorgyan, T. Tromholt, B. Andreasen, F.C. Krebs, Adv. Mater. 24 (2012) 580.
[11] H. Cao, M. Tanaka, K. Ishikawa, Appl. Phys. Lett. 103 (2013) 143305.
[12] M. Jin Tan, S. Zhong, R. Wang, Z. Zhang, V. Chellappan, W. Chen, Appl. Phys. Lett. 103 (2013) 063303.
[13] A.A. Bakulin, A. Rao, V.G. Pavelyev, P.H.M. van Loosdrecht, M.S. Pshenichnikov, D. Niedzialek, J. Cornil, D. Beljonne, R.H. Friend, Science 335 (2012) 1340.
[14] A.E. Jailaubekov, A.P. Willard, J.R. Tritsch, W.-L. Chan, N. Sai, R. Gearba, L.G. Kaake, K.J. Williams, K. Leung, P.J. Rossky, X.Y. Zhu, Nat. Mater. 12 (2013) 66.
[15] K.K. Ishibashi, Y. Kimura, M. Niwano, J. Appl. Phys. 103 (2008) 94507.
[16] C.F. Zhang, J.C. Zhang, Y. Hao, Z.H. Lin, C.X. Zhu, J. Appl. Phys. 110 (2011) 64504.
[17] P. Schilinsky, C. Waldauf, J. Hauch, C.J. Brabec, J. Appl. Phys. 95 (2004) 2816.
[18] B. Qi, J. Wang, Phys. Chem. Chem. Phys. 15 (2013) 8972.
[19] B. Qi, J. Wang, J. Mater. Chem. 22 (2012) 24315.
[20] M.C. Scharber, D. Wuhlbacher, M. Koppe, P. Denk, C. Waldauf, A.J. Heeger, C.L. Brabec, D. Mühlbacher, Adv. Mater. 18 (2006) 789.
[21] G. Chen, H. Sasabe, Z. Wang, X. Wang, Z. Hong, Y. Yang, J. Kido, Adv. Mater. 24 (2012) 2768.
[22] K. Sakai, M. Hiramoto, Mol. Cryst. Liq. Cryst. 491 (2008) 284.
[23] J. Wagner, M. Gruber, A. Hinderhofer, A. Wilke, B. Bröker, J. Frisch, P. Amsalem, A. Vollmer, A. Opitz, N. Koch, F. Schreiber, W. Brütting, Adv. Funct. Mater. 20 (2010) 4295.
[24] K. Norrman, M.V. Madsen, S.A. Gevorgyan, F.C. Krebs, J. Am. Chem. Soc. 132 (2010) 16883.
[25] M.O. Reese, A.J. Morfa, M.S. White, N. Kopidakis, S.E. Shaheen, G. Rumbles, D.S. Ginley, Sol. Energy Mater. Sol. Cells 92 (2008) 746.
[26] C. Schmidt, in: G. Gerlach, K.-J. Wolter (Eds.), Bio Nano Packag. Tech. Electron Devices, Springer-Verlag, Berlin Heidelberg, 2012, pp. 586–589.
[27] D.E. Motaung, G.F. Malgas, C.J. Arendse, J. Mater. Sci. 46 (2011) 4942.
[28] S.O. Jeon, J. Yeob, J.Y. Lee, Sol. Energy Mater. Sol. Cells 101 (2012) 160.
[29] H. Hoppe, N.S. Sariciftci, J. Mater. Chem. 16 (2006) 45.
[30] B. Ray, M.A. Alam, Appl. Phys. Lett. 99 (2011) 333031.
[31] R. Franke, B. Maennig, A. Petrich, M. Pfeiffer, Sol. Energy Mater. Sol. Cells 92 (2008) 732.
[32] M.L. Wang, Q.L. Song, H.R. Wu, B.F. Ding, X.D. Gao, X.Y. Sun, X.M. Ding, X.Y. Hou, Org. Electron. 8 (2007) 445.
[33] J.J. Kim, S. Kwak, J.-S. Yu, Y. Jang, J. Jo, T. Lee, I. Kim, Appl. Phys. Lett. 101 (2012) 213304.
[34] M. Hermenau, M. Riede, K. Leo, S.A. Gevorgyan, F.C. Krebs, K. Norrman, Sol. Energy Mater. Sol. Cells 95 (2011) 1268.
[35] F. Yan, J. Noble, J. Peltola, S. Wicks, S. Balasubramanian, Sol. Energy Mater. Sol. Cells 114 (2013) 214.
[36] A.V. Hamza, J. Dykes, W.D.D. Mosley, L. Dinh, M. Balooch, Surf. Sci. 318 (1994) 368.
[37] H. Habuchi, S. Nitta, D.X. Han, S. Nonomura, J. Appl. Phys. 87 (2000) 8580.
[38] H. Ishii, K. Seki, IEEE Trans. Electron Devices 44 (1997) 1295.
[39] M.T. Lloyd, D.C. Olson, P. Lu, E. Fang, D.L. Moore, M.S. White, M.O. Reese, D.S. Ginley, J.W.P. Hsu, J. Mater. Chem. 19 (2009) 7638.
[40] Q.L. Song, M.L. Wang, E.G. Obbard, X.Y. Sun, X.M. Ding, X.Y. Hou, C.M. Li, Appl. Phys. Lett. 89 (2006) 251113.
[41] A. Seemann, H.J. Egelhaaf, C.J. Brabec, J.A. Hauch, Org. Electron. 10 (2009) 1424.
[42] E. Wahlström, E.K. Vestergaard, R. Schaub, A. Rønnau, M. Vestergaard, E. Laegsgaard, I. Stensgaard, F. Besenbacher, Science 303 (2004) 511.
[43] M. Lira-Cantu, K. Norrman, J.W. Andreasen, N. Casan-Pastor, F.C. Krebs, J. Electrochem. Soc. 154 (2007) B508.
[44] M. Lira-Cantu, K. Norrman, J.W. Andreasen, F.C. Krebs, Chem. Mater. 18 (2006) 5684.
[45] F.C. Krebs, T. Tromholt, M. Jørgensen, Nanoscale 2 (2010) 873.
[46] X. Xi, W.J. Li, J.Q. Wu, J.J. Ji, Z.R. Shi, G.H. Li, Sol. Energy Mater. Sol. Cells 94 (2010) 2435.
[47] F.C. Krebs, M. Jørgensen, K. Norrman, O. Hagemann, J. Alstrup, T.D. Nielsen, J. Fyenbo, K. Larsen, J. Kristensen, Sol. Energy Mater. Sol. Cells 93 (2009) 422.
[48] M.J. Tan, S. Zhong, J. Li, Z. Chen, W. Chen, ACS Appl. Mater. Interfaces 5 (2013) 4696.
[49] B. Andreasen, D.M. Tanenbaum, M. Hermenau, E. Voroshazi, M.T. Lloyd, Y. Galagan, B. Zimmernann, S. Kudret, W. Maes, L. Lutsen, D. Vanderzande, U. Würfel, R. Andriessen, R. Rösch, H. Hoppe, G. Teran-Escobar, M. Lira-Cantu, A. Rivaton, G.Y. Uzunoğlu, D.S. Germack, M. Hösel, H.F. Dam, M. Jørgensen, S.A. Gevorgyan, M.V. Madsen, E. Bundgaard, F.C. Krebs, K. Norrman, Phys. Chem. Chem. Phys. 14 (2012) 11780.
[50] C.C. Eloi, J.D. Robertson, A.M. Rao, P. Zhou, K.-A. Wang, P.C. Eklund, D.J. Robertson, J. Mater. Res. 8 (1993) 3085.
[51] M. Tavakkoli, R. Ajeian, M.N. Badrabadi, S.S. Ardestani, S.M.H. Feiz, K.E. Nasab, Sol. Energy Mater. Sol. Cells 95 (2011) 1964.
[52] R. Roesch, M. Seeland, M. Bärenklau, G. Gobsch, H. Hoppe, Sol. Energy Mater. Sol. Cells 111 (2013) 212.
[53] K. Kawano, R. Pacios, D. Poplavskyy, J. Nelson, D.D.C. Bradley, J.R. Durrant, Sol. Energy Mater. Sol. Cells 90 (2006) 3520.
[54] K. Norrman, S.A. Gevorgyan, F.C. Krebs, ACS Appl. Mater. Interfaces 1 (2009) 102.
[55] M.H. Petersen, S.A. Gevorgyan, F.C. Krebs, Macromolecules 41 (2008) 8986.
[56] E. Voroshazi, B. Verreet, A. Buri, R. Müller, D. Di Nuzzo, P. Heremans, Org. Electron. 12 (2011) 736.
[57] M.M.-C. Chen, Y.Y.-S. Chiou, J.-M.J. Chiu, A. Tedla, Y. Tai, J. Mater. Chem. A 1 (2013) 3680.
[58] T. Yamanari, T. Taima, J. Sakai, J. Tsukamoto, Y. Yoshida, Jpn. J. Appl. Phys. 49 (2010) 01AC02.
[59] Y. Sun, C.J. Takacs, S.R. Cowan, J.H. Seo, X. Gong, A. Roy, A.J. Heeger, Adv. Mater. 23 (2011) 2226.
[60] M. Hermenau, S. Schubert, H. Klumbies, J. Fahlteich, L. Müller-Meskamp, K. Leo, M. Riede, Sol. Energy Mater. Sol. Cells 97 (2012) 102.
[61] H.R. Wu, Q.L. Song, M.L. Wang, F.Y. Li, H. Yang, Y. Wu, C.H. Huang, X.M. Ding, X.Y. Hou, Thin Solid Films 515 (2007) 8050.
[62] J.U. Lee, J.W. Jung, J.W. Jo, W.H. Jo, J. Mater. Chem. 22 (2012) 24265.
[63] K. Norrman, N.B. Larsen, F.C. Krebs, Sol. Energy Mater. Sol. Cells 90 (2006) 2793.
[64] H. Cao, K. Ishikawa, Sol. Energy Mater. Sol. Cells 109 (2013) 215.
[65] T. Tromholt, A. Manor, E.A. Katz, F.C. Krebs, Nanotechnology 22 (2011) 225401.
[66] E.A. Katz, S. Gevorgyan, M.S. Orynbayev, F.C. Krebs, Eur. Phys. J. Appl. Phys. 36 (2006) 307.
[67] J.W. Arbogast, A.P. Darmanyan, C.S. Foote, F.N. Diederich, R.L. Whetten, Y. Rubin, M.M. Alvarez, S.J. Anz, J. Phys. Chem. 95 (1991) 11.
[68] J.M. Wessels, M.A.J. Rodgers, J. Phys. Chem. 99 (1995) 17586.
[69] S.J. Duclos, R.C. Haddon, S.H. Glarum, A.F. Hebard, K.B. Lyons, Solid State Commun. 80 (1991) 481.
[70] M. Jaime, M. Nuñez Regueiro, M. Jaimc, M. Nuñez Regueiro, Appl. Phys. A Mater. Sci. Process. 60 (1995) 289.
[71] Y. Zhou, C. Fuentes-Hernandez, J. Shim, J. Meyer, A.J. Giordano, H. Li, P. Winget, T. Papadopoulos, H. Cheun, J. Kim, M. Fenoll, A. Dindar, W. Haske, E. Najafabadi, T.M. Khan, H. Sojoudi, S. Barlow, S. Graham, J.-L. Brédas, S.R. Marder, A. Kahn, B. Kippelen, Science 336 (2012) 327.
[72] M.W. Rowell, M.A. Topinka, M.D. McGehee, H.-J. Prall, G. Dennler, N.S. Sariciftci, L. Hu, G. Gruner, Appl. Phys. Lett. 88 (2006) 233506.
[73] M. Manceau, E. Bundgaard, J.E. Carle, O. Hagemann, M. Helgesen, R. Sondergaard, M. Jørgensen, F.C. Krebs, J. Mater. Chem. 21 (2011) 4132.
[74] M.O. Reese, M.S. White, G. Rumbles, D.S. Ginley, S.E. Shaheen, Appl. Phys. Lett. 92 (2008) 53303.
[75] B. Zimmermann, U. Würfel, M. Niggemann, Sol. Energy Mater. Sol. Cells 93 (2009) 491.
[76] M. Wang, F. Xie, J. Du, Q. Tang, S. Zheng, Q. Miao, J. Chen, N. Zhao, J.B. Xu, Sol. Energy Mater. Sol. Cells 95 (2011) 3303.
[77] W.R. Mateker, J.D. Douglas, C. Cabanetos, I.T. Sachs-Quintana, J. a Bartelt, E.T. Hoke, A. El Labban, P.M. Beaujuge, J.M.J. Fréchet, M.D. McGehee, Energy Environ. Sci. 6 (2013) 2529.
[78] K. Lee, J.Y. Kim, S.H. Park, S.H. Kim, S. Cho, A.J. Heeger, Adv. Mater. 19 (2007) 2445.
[79] J. Li, S. Kim, S. Edington, J. Nedy, S. Cho, K. Lee, A.J. Heeger, M.C. Gupta, J.T. Yates, Sol. Energy Mater. Sol. Cells 95 (2011) 1123.
[80] H. Hänsel, H. Zettl, G. Krausch, C. Schmitz, R. Kisselev, M. Thelakkat, H.-W. Schmidt, Appl. Phys. Lett. 81 (2002) 2106.
[81] J. You, C.-C. Chen, L. Dou, S. Murase, H.-S. Duan, S.A. Hawks, T. Xu, H.J. Son, L. Yu, G. Li, Y. Yang, Adv. Mater. 24 (2012) 5267.
[82] H. Saarenpää, T. Niemi, A. Tukiainen, H. Lemmetyinen, N. Tkachenko, Sol. Energy Mater. Sol. Cells 94 (2010) 1379.

[83] O. Pachoumi, C. Li, Y. Vaynzof, K.K. Banger, H. Sirringhaus, Adv. Energy Mater. (2013).
[84] H. Liu, Z. Wu, J. Hu, Q. Song, B. Wu, H. Lam Tam, Q. Yang, W. Hong Choi, F. Zhu, Appl. Phys. Lett. 103 (2013) 043309.
[85] H. Jin, C. Tao, M. Velusamy, M. Aljada, Y. Zhang, M. Hambsch, P.L. Burn, P. Meredith, Adv. Mater. (2012) 2572.
[86] K.-S. Chen, J.-F. Salinas, H.-L. Yip, L. Huo, J. Hou, A.K.-Y. Jen, Energy Environ. Sci. 5 (2012) 9551.
[87] Z. Zhang, Y. Xiao, H.-X. Wei, G.-F. Ma, S. Duhm, Y.-Q. Li, J.-X. Tang, Appl. Phys. Express 6 (2013) 095701.
[88] R. Rösch, D.M. Tanenbaum, M. Jørgensen, M. Seeland, M. Bärenklau, M. Hermenau, E. Voroshazi, M.T. Lloyd, Y. Galagan, B. Zimmermann, U. Würfel, M. Hösel, H.F. Dam, S.A. Gevorgyan, S. Kudret, W. Maes, L. Lutsen, D. Vanderzande, R. Andriessen, G. Teran-Escobar, M. Lira-Cantu, A. Rivaton, G.Y. Uzunoğlu, D. Germack, B. Andreasen, M.V. Madsen, K. Norrman, H. Hoppe, F.C. Krebs, Energy Environ. Sci. 5 (2012) 6521.
[89] H. Cao, H. Takezoe, K. Ishikawa, Jpn. J. Appl. Phys. 52 (2013) 40202.
[90] C. Leyens, in: C. Leyens, M. Peters (Eds.), Wiley-VCH, Weinheim, 2003, p. 189, 199 and 213.
[91] G. Lütjering, J.C. Williams, Titanium, Springer, Berlin, 2007.
[92] Z. Liu, G. Welsch, Metall. Trans. A 19 (1988) 1121.
[93] L.S. Dake, R.J. Lad, Surf. Sci. 289 (1993) 297.
[94] Q. Sun, Q. Wang, P. Jena, Y. Kawazoe, J. Am. Chem. Soc. 127 (2005) 14582.
[95] R.C. Haddon, A.F. Hebard, M.J. Rosseinsky, D.W. Murphy, S.J. Duclos, K.B. Lyons, B. Miller, J.M. Rosamilia, R.M. Fleming, A.R. Kortan, S.H. Glarum, A.V. Makhija, A.J. Muller, R.H. Eick, S.M. Zahurak, R. Tycko, G. Dabbagh, F.A. Thiel, Nature 350 (1991) 320.
[96] Q.L. Song, F.Y. Li, H. Yang, H.R. Wu, X.Z. Wang, W. Zhou, J.M. Zhao, X.M. Ding, C.H. Huang, X.Y. Hou, Chem. Phys. Lett. 416 (2005) 42.
[97] B.J. Worfolk, T.C. Hauger, K.D. Harris, D.A. Rider, J.A.M. Fordyce, S. Beaupré, M. Leclerc, J.M. Buriak, Adv. Energy Mater. 2 (2012) 361.
[98] M. Song, J.-W. Kang, D.-H. Kim, J.-D. Kwon, S.-G. Park, S. Nam, S. Jo, S.Y. Ryu, C.S. Kim, Appl. Phys. Lett. 102 (2013) 143303.
[99] M.O. Reese, S.A. Gevorgyan, M. Jørgensen, E. Bundgaard, S.R. Kurtz, D.S. Ginley, D.C. Olson, M.T. Lloyd, P. Morvillo, E.A. Katz, A. Elschner, O. Haillant, T.R. Currier, V. Shrotriya, M. Hermenau, M. Riede, K.R. Kirov, G. Trimmel, T. Rath, O. Inganäs, F. Zhang, M. Andersson, K. Tvingstedt, M. Lira-Cantu, D. Laird, C. McGuiness, S. (Jimmy) Gowrisanker, M. . Pannone, M. . Xiao, J. . Hauch, R. . Steim, D.M. . DeLongchamp, R. . Rösch, H. . Hoppe, N. . Espinosa, A. Urbina, G. . Yaman-Uzunoglu, J.-B. . Bonekamp, A.J.J.M. . van Breemen, C. Girotto, E. Voroshazi, F.C. Krebs, Sol. Energy Mater. Sol. Cells 95 (2011) 1253.
[100] J. Burschka, N. Pellet, S.-J. Moon, R. Humphry-Baker, P. Gao, M.K. Nazeeruddin, M. Grätzel, Nature 499 (2013) 316.
[101] M. Hermenau, S. Scholz, K. Leo, M. Riede, Sol. Energy Mater. Sol. Cells 95 (2011) 1278.
[102] G. Williams, Q. Wang, H. Aziz, Adv. Funct. Mater. 23 (2013) 2239.
[103] Y.-J. Kang, K. Lim, S. Jung, D.-G. Kim, J.-K. Kim, C.-S. Kim, S.H. Kim, J.-W. Kang, Sol. Energy Mater. Sol. Cells 96 (2012) 137.
[104] C. Lungenschmied, G. Dennler, H. Neugebauer, S.N. Sariciftci, M. Glatthaar, T. Meyer, A. Meyer, Sol. Energy Mater. Sol. Cells 91 (2007) 379.
[105] F.C. Krebs, Sol. Energy Mater. Sol. Cells 90 (2006) 3633.
[106] D. Angmo, S.A. Gevorgyan, T.T. Larsen-Olsen, R.R. Søndergaard, M. Hösel, M. Jørgensen, R. Gupta, G.U. Kulkarni, F.C. . Krebs, Org. Electron. 14 (2013) 984.
[107] R. Tipnis, J. Bernkopf, S. Jia, J. Krieg, S. Li, M. Storch, D. Laird, Sol. Energy Mater. Sol. Cells 93 (2009) 442.
[108] S.R. Ferreira, P. Lu, Y. Lee, R.J. Davis, J.W.P. Hsu, J. Phys. Chem. C 115 (2011) 13471.
[109] S. Ebadian, B. Gholamkhass, S. Shambayati, S. Holdcroft, P. Servati, Sol. Energy Mater. Sol. Cells 94 (2010) 2258.
[110] S.-C. Chien, F.-C. Chen, M.-K. Chung, C.-S. Hsu, J. Phys. Chem. C 116 (2011) 1354.
[111] A. Hayakawa, O. Yoshikawa, T. Fujieda, K. Uehara, S. Yoshikawa, Appl. Phys. Lett. 90 (2007) 163517.
[112] J.Y. Kim, K. Lee, N.E. Coates, D. Moses, T.Q. Nguyen, M. Dante, A.J. Heeger, Science 317 (2007) 222.
[113] S.K. Hau, H.-L. Yip, N.S. Baek, J. Zou, K. O'Malley, A.K.-Y.Y. Jen, Appl. Phys. Lett. 92 (2008) 253301.
[114] Y. Liang, Z. Xu, J. Xia, S.-T. Tsai, Y. Wu, G. Li, C. Ray, L. Yu, Adv. Mater. 22 (2010) E135.
[115] A. Arlauskas, M. Pranaitis, R. Lessmann, M. Riede, K. Leo, V. Kaz, V. Kazukauskas, Opt. Mater. (Amst.) 32 (2010) 1676.
[116] P. Vivo, J. Jukola, M. Ojala, V. Chukharev, H. Lemmetyinen, Sol. Energy Mater. Sol. Cells 92 (2008) 1416.
[117] W.J. Potscavage, S. Yoo, B. Domercq, B. Kippelen, Appl. Phys. Lett. 90 (2007) 253511.